Inorganic Chemistry

pubs.acs.org/IC Article

Fitting Multiplet Simulations to L-Edge XAS Spectra of Transition-Metal Complexes Using an Adaptive Grid Algorithm

María G. Herrera-Yáñez, J. Alberto Guerrero-Cruz, Mahnaz Ghiasi, Hebatalla Elnaggar, Andrea de la Torre-Rangel, L. Alejandra Bernal-Guzmán, Roberto Flores-Moreno, Frank M. F. de Groot, and Mario U. Delgado-Jaime*

Cite This: *Inorg. Chem.* 2023, 62, 3738–3760 Read Online

ACCESS | Metrics & More | Article Recommendations | Supporting Information

ABSTRACT: A new methodology based on an adaptive grid algorithm followed by an analysis of the ground state from the fit parameters is presented to analyze and interpret experimental XAS $L_{2,3}$-edge data. The fitting method is tested first in a series of multiplet calculations for d^0−d^7 systems and for which the solution is known. In most cases, the algorithm is able to find the solution, except for a mixed-spin Co^{2+} O_h complex, where it instead revealed a correlation between the crystal field and the electron repulsion parameters near spin-crossover transition points. Furthermore, the results for the fitting of previously published experimental data sets on CaO, CaF_2, MnO, $LiMnO_2$, and Mn_2O_3 are presented and their solution discussed. The presented methodology has allowed the evaluation of the Jahn−Teller distortion in $LiMnO_2$, which is consistent with the observed implications in the development of batteries, which use this material. Moreover, a follow-up analysis of the ground state in Mn_2O_3 has demonstrated an unusual ground state for the highly distorted site which would be impossible to optimize in a perfect octahedral environment. Ultimately, the presented methodology can be used in the analysis of X-ray absorption spectroscopy data measured at the $L_{2,3}$-edge for a large number of materials and molecular complexes of first-row transition metals and can be expanded to the analysis of other X-ray spectroscopic data in future studies.

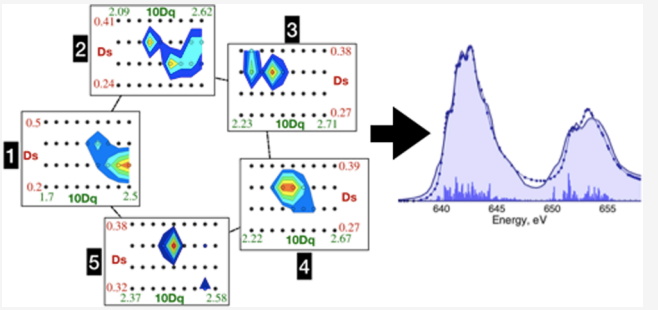

INTRODUCTION

X-ray absorption spectroscopy (XAS) is an important experimental tool to study the electronic structure of numerous materials and of molecular systems based on transition metals.[1,2] XAS is an element-specific technique that can map their corresponding contributions into low-lying empty molecular orbitals. In particular, metal $L_{2,3}$-edge XAS involves the transition of a core electron from a 2p orbital in a transition metal to molecular orbitals that are rich in metal-3d character.[1] As it is subject to multiplet effects, the detailed interpretation depends largely on our ability to calculate multiple electronic states. Multiplet simulations are a relatively inexpensive method to analyze X-ray data which have evolved over time to incorporate different electronic structure effects relevant to many body systems such as electron−electron interactions, spin−orbit coupling, crystal-field interactions and charge transfer multiplet effects to account for bonding interactions.[1,3−8] In this work we discuss the development of a methodology for the automatic fitting of crystal field multiplet simulations to calculated data sets in d^0−d^7 systems and to experimental $L_{2,3}$-edge XAS of calcium compounds and manganese oxides and the implementation of this methodology in BlueprintXAS, software originally developed to fit empirical models to X-ray data, with the purpose of reducing user bias on the starting point and of evaluating uncertainties in fitting parameters.[9,10] The parameters optimized using this methodology are the radial parameters $F^k_{3d,3d}$, $G^k_{3d,3d}$, $10D_q$, D_s, and D_t, using an adaptive grid algorithm discussed in the next section. Originally, multiplet simulations were formulated to reproduce the X-ray spectra of metal and transition-metal oxides.[1,11] It was based on the treatment of local metallic sites within the structure of solids, ignoring intermetallic interactions, and involving only atomic interactions: namely, electron−electron interactions and spin−orbit coupling. Then later on, also crystal-field interactions are introduced based on the point-charge model originally proposed by Bethe and van Vleck.[12,13] This simple formulation was able to capture the structure of X-ray absorption spectra of oxides at the $L_{2,3}$-edge (involving electric dipole transitions from core electrons

Received: August 7, 2022
Published: February 21, 2023

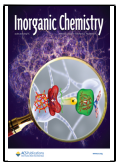

in 2p shells to valence 3d shells of transition metals). Despite being a calculation involving multiple electronic states (multiconfigurational in nature), multiplet simulations are inexpensive computationally, as they rely on the use of empirical parameters, even though the physics describing the interactions at the metallic sites is fairly complete.

Over the years, this method has been expanded to study the electronic structure of covalent materials,[5,6,14,15] of molecular transition-metal complexes,[16−19] and of biological systems using the charge-transfer multiplet model.[20−22] This model was first applied to interpret XPS 2p data of covalent materials based on transition metals to account for additional spectral features that were observed which could not be accounted for using the crystal field multiplet model.[23−25] Later, the method was extended to analyze the $L_{2,3}$-edge XAS data of covalent solids and transition-metal complexes in chemistry and biology. For molecular systems, the method has been used to interpret the experimental data of transition-metal complexes containing not only donor ligands but also acceptor ligands.[17,19] The method has been successfully used to analyze $L_{2,3}$-edge-like cuts from 1s2p RIXS data collected in biological samples,[21] and recent developments have allowed an analysis of systems where the local symmetry of the metallic sites are subject to 4p−3d hybridization of the metal orbitals.[22] All of these developments make use of the original Cowan codes in conjunction with the codes later developed by Butler and Thole to mix charge transfer states.[14,15,26] They also use the projection method originally described by Wasinger et al. to extract differential orbital covalency[16] to be able to compare fit simulations to DFT models. In addition, other groups have developed their own codes with different purposes.[7,8,27−31] More recent developments include approaches based on first principles with the advantage of relying on structural models and much less on empirical parameters, even though they could be more expensive computationally.[32−37] Herein, we developed our own code in Matlab to be able to optimize the internal processes of diagonalization of the initial and final states with the idea of directly optimizing scaling factors, global shifts, and broadening parameters using our optimizer BlueprintXAS. The approach of calculating the spectra is similar to that of Cowan, and the construction of operators is analogous to that of Quanty in the sense that each operator is represented as a matrix whose size depends on the number of microstates in the initial and final configurations. Moreover, we developed an adaptive grid algorithm capable of finding the right combination of parameters that fit the $L_{2,3}$-edge XAS of transition-metal complexes. This algorithm consists of the creation of an initial grid that is built with all the simulation parameters ranging from lower to upper limits in step sizes defined by the user. Based on the calculation of the spectra from all combinations in the grid and the fitting of additional parameters using a nonlinear least-squares method in each case, the algorithm then calculates new grids in subsequent cycles with increased precision for each parameter. We demonstrate the applicability of the method on finding unique solutions in many d^0−d^7 systems, and we also show when the method leads to find multiple solutions whenever applicable. We note here that the work presented represents a first step in the development of a more comprehensive version that includes charge transfer effects and 3d−4p hybridization, both of which may be important in other spectroscopies for covalent systems.

The approach presented here can be of great value to many scientists in different fields who seek to obtain the electronic structures of different materials and molecular systems directly from experimental data but have encountered a challenge in finding the right combination of parameters so that the multiplet simulation properly fits the experimental spectra. In this regard, another complication is the fact that finding a combination of parameters does not necessarily ensure that this would be the only solution. That is, since the experimental data are obtained with only a certain resolution, there is an uncertainty associated with each parameter that ideally needs to be evaluated. We tested this by first fitting calculated data sets for which we know the solution in two different scenarios: one in which the calculations are broadened with a half-width at half-maximum (hwhm) of 0.3 eV and another in which the hwhm parameter is set to 0.8 eV. Our method allows not only the calculation of uncertainties for each radial parameter but also the possibility of exploring a large solution space where other solutions may be possible, which would depend largely on how structured the experimental data are to begin with. To test that the algorithm is capable of finding the solution starting with a large solution space, we fit calculated data sets in d^0-d^7 systems based on Ti, V, Cr, Fe, and Co in different environments for which the solution is known in advance. We further fit multiplet simulations in previously documented experimental data sets. We highlight here the solution found for $LiMnO_2$, which to our knowledge is the best solution found so far from XAS for this material. This involved the optimization of five radial parameters: that is, the scaling factor for the Slater integrals $F^k_{3d,3d}$, the scaling factor for $F^k_{2p,3d}$ and $G^k_{2p,3d}$, and the crystal field parameters $10D_q$, D_s, and D_t. From the solution found, we get a better idea of its electronic structure which implies a large Jahn−Teller distortion responsible for the challenges associated with swelling when using this material in lithium batteries, in contrast to the use of batteries based on cobalt, which are not as sustainable.[38−40] This example further illustrates that, for a material subject to Jahn−Teller distortions, finding a solution manually could be challenging and the prospect of relying on an automatic method to do so is of great value.

Finally, we also emphasize here that the method can be also quite useful to study composite materials where more than one site of the same metal can contribute to the XAS spectrum and where the composition parameters are free-floating parameters that can be optimized with infinite precision using our methodology. We illustrate this in the analysis of the calculated data for a mixed-valence material analogous to Prussian blue and also in the analysis of the data for Mn_2O_3, containing two different Mn^{3+} sites.

The present study focuses on the analysis of XAS data at the $L_{2,3}$-edge of materials based on transition-metal complexes which are predominantly ionic in nature and for which we fit crystal field multiplet simulations (instead of charge transfer multiplet simulations). However, the same approach can be extended to optimize charge-transfer and 4p−3d hybridization parameters so that molecular systems in chemistry and biology can be studied by fitting charge-transfer multiplet simulations not only to XAS data but also to other X-ray spectroscopy data available.

MATERIALS AND METHODS

Calculation of Electronic States in the Initial and Final Configurations Using Crystal-Field Multiplet Simulations. The

https://doi.org/10.1021/acs.inorgchem.2c02830
Inorg. Chem. 2023, 62, 3738−3760

electron−electron interaction Hamiltonians $\frac{e^2}{r_{ij}}$ between any two electrons, namely i and j and the crystal-field interaction of 3d electrons in the metal and N point charges at distances of a_i from the metal are modeled using a multipole expansion in terms of a complete series of spherical harmonic.[3,13,41]

$$\frac{e^2}{r_{ij}} = e^2 \sum_{k=0}^{\infty} \sum_{m=-k}^{+k} \frac{r_<^k}{r_>^{k+1}} (-1)^m C_k^{-m}(\theta_i, \phi_i) C_k^m(\theta_j, \phi_j) \tag{1}$$

$$\hat{V}^{\mathrm{CF}} = ze^2 \sum_{k=0}^{\infty} \frac{r^k}{a^{k+1}} \sum_{m=-k}^{+k} A_{km} C_k^m(\theta, \phi) \tag{2}$$

where $C_k^m(\theta,\varphi)$ represent weighted normalized spherical harmonics with

$$C_k^m(\theta, \phi) = \sqrt{\frac{4\pi}{2k+1}} Y_k^m(\theta, \phi) \tag{3}$$

In the case of the electron−electron repulsion potential, the operator $\frac{e^2}{r_{ij}}$ in eq 1 is now a function of the separated coordinates of electron i (r_i, θ_i, ϕ_i) and electron j (r_j, θ_j, ϕ_j) which allows the evaluation of matrix elements in the domain of each of these electrons. We note here that $r_>$ represents the maximum between r_i and r_j (that is, the maximum distance to the nucleus between that of electron i and that of electron j). Similarly, $r_<$ represents the minimum between r_i and r_j. This implies the evaluation of two integrals while evaluating matrix elements from expression 1, one for all points (r_i, r_j) at which $r_> = r_i$ and $r_< = r_j$ and another for all points at which $r_> = r_j$ and $r_< = r_i$. In the case of eq 2 corresponding to the crystal field potential, the coordinates r, θ, and ϕ correspond to a 3d electron in the transition metal and the expansion coefficients A_{km} are obtained by adding together the value of the normalized spherical harmonic, $(-1)^m C_k^{-m}(\theta, \varphi)$ evaluated at every location of the N point charges. That is

$$A_{km} = \sum_{i=1}^{N} (-1)^m C_k^{-m}(\theta_i, \varphi_i) \tag{4}$$

The infinite expansions from eqs 1 and 2 get quickly truncated by the symmetry properties of integrals of three spherical harmonics, which restricts the values of k to be 0, 2, or 4 for nonvanishing terms in the case of 3d electrons. Further symmetry restrictions under the symmetry of the metal complex, which vanishes all terms containing spherical harmonics not transformed as the totally symmetric irreducible representation, significantly reduce the number of terms in the final crystal field potential $\hat{V}^{\mathrm{CF}}$. In the case of a perfect octahedral field with 6 point charges located at a distance a from the metal center, eq 2 reduces to,

$$\hat{V}_{O_h}^{\mathrm{CF}} = \frac{ze^2 r^4}{a^5} \times \frac{7}{2}\left(C_4^0 + \sqrt{\frac{5}{14}} C_4^{-4} + \sqrt{\frac{5}{14}} C_4^4\right) \tag{5}$$

whereas the crystal field of an octahedral complex under a tetragonal distortion, which elongates or compress two of the charges located in the z axis to distance b from the metal center, thus allows additional terms by breaking the O_h symmetry to D_{4h}

$$\hat{V}_{D_{4h}}^{\mathrm{CF}} = \frac{z_a e^2 r^4}{a^5} \times \frac{7}{2}\left(C_4^0 + \sqrt{\frac{5}{14}} C_4^{-4} + \sqrt{\frac{5}{14}} C_4^4\right) - e^2\left(\frac{z_a r^2}{a^3} - \frac{z_b r^2}{b^3}\right) \times 2(C_2^0) - e^2\left(\frac{z_a r^4}{a^5} - \frac{z_b r^4}{b^5}\right) \times 2(C_4^0) \tag{6}$$

Moreover, considering XAS $L_{2,3}$-edge spectroscopy, the other important atomic interactions at play are the spin−orbit coupling for the 2p and 3d electrons, which are calculated from the Hamiltonian

$$\hat{H}^{\mathrm{SOC}} = \xi_{nl} \hat{l}\cdot\mathbf{s} = \frac{\xi_{nl}}{2}(\hat{j}^2 - \hat{l}^2 - \hat{s}^2) = \xi_{nl}\left(\hat{l}_z\hat{s}_z + \frac{\hat{l}_+\hat{s}_- + \hat{l}_-\hat{s}_+}{2}\right) \tag{7}$$

Thus, the total Hamiltonian in the initial state $|3d^n\rangle$ is

$$\hat{H}^{\mathrm{INITIAL}} = \sum_i^n \left(-\frac{\hbar^2}{2m_e}\nabla_i^2 - \frac{Ze^2}{r_i}\right) + \sum_i^n \sum_{j>i}^n \frac{e^2}{r_{ij}} + \sum_i^n \hat{V}_i^{CF} + \xi_{3d} \sum_i^n l_i\cdot\mathbf{s}_i \tag{8}$$

whereas the Hamiltonian in the final state $|2p^5 3d^{n+1}\rangle$ is

$$\hat{H}^{\mathrm{FINAL}} = \sum_i^{n+6} \left(-\frac{\hbar^2}{2m_e}\nabla_i^2 - \frac{Ze^2}{r_i}\right) + \sum_i^{n+6} \sum_{j>i}^{n+6} \frac{e^2}{r_{ij}} + \sum_i^{n+1} \hat{V}_i^{CF} + \xi_{2p} \sum_i^5 l_i\cdot\mathbf{s}_i + \xi_{3d} \sum_i^{n+1} l_i\cdot\mathbf{s}_i \tag{9}$$

Thus, the task at play then is to obtain matrix elements from Hamiltonians (8) and (9) applied over all microstates in the initial $|3d^n\rangle$ and final $|2p^5 3d^{n+1}\rangle$ states, recognizing that the obtained matrices $\mathbf{H}^{\mathrm{INITIAL}}$ and $\mathbf{H}^{\mathrm{FINAL}}$ can be formulated as a sum of angular matrices comprising each type of interaction multiplied by the corresponding radial parameter

$$\mathbf{H}^{INITIAL} = \square F^0_{3d,3d} + \square F^2_{3d,3d} + \square F^4_{3d,3d} + \square 10Dq + \square Ds + \square Dt + \square \xi_{3d} \tag{10}$$

$$\mathbf{H}^{FINAL} = \square F^0_{3d,3d} + \square F^2_{3d,3d} + \square F^4_{3d,3d} + \square F^0_{2p,3d} + \square F^2_{2p,3d} + \square G^1_{2p,3d} + \square G^3_{2p,3d} + \square 10Dq + \square Ds + \square Dt + \square \xi_{3d} + \square \xi_{2p} \tag{11}$$

where $F^0_{3d,3d}$ and $F^0_{2p,3d}$ are chosen to center the multiplets around the average energy of the initial or final states with

$$F^0_{3d,3d} = E_{ave} + \frac{2}{63}(F^2_{3d,3d} + F^4_{3d,3d}) \tag{12}$$

$$F^0_{2p,3d} = E_{ave} + \frac{1}{15}G^1_{2p,3d} + \frac{3}{70}G^3_{2p,3d} \tag{13}$$

The graphical representations in eqs 10 and 11 imply larger-sized matrices for the final state than for the initial state. The actual size of the matrices depends on the number of microstates in the initial $3d^N$ and final $2p^5 3d^{N+1}$ state configurations.

Table 1 gives the number of microstates in the initial and final states for initial state configurations $3d^0$−$3d^9$. In our code, the angular matrices depicted in color in eqs 10 and 11 for the different interactions are calculated once and then stored. Then they are used for crystal-field multiplet simulations by simply varying the radial parameters, amplifying each matrix containing the angular part. The diagonalization of matrices in eqs 10 and 11 then provides the electronic states in each configuration as linear combinations of microstates and corresponding energies as their eigenvalues.

Definition of Radial Parameters. The radial parameters, known as Slater integrals, can in principle be computed from 3d and 2p radial functions. These include $F^2_{3d,3d}$ and $F^4_{3d,3d}$, (accounting for Coulomb interactions between 3d electrons at the metal), $F^2_{3p,3d}$ (accounting for direct coulomb interactions between 2p and 3d electrons at the metal), and $G^1_{2p,3d}$, $G^3_{2p,3d}$ (accounting for exchange interactions between 2p and 3d electrons at the metal). In addition, $F^0_{3d,3d}$ and

https://doi.org/10.1021/acs.inorgchem.2c02830
Inorg. Chem. 2023, 62, 3738−3760

Table 1. Number of Microstates in the Initial ($2p^63d^N$) and Final ($2p^53d^{N+1}$) State Configurations Involved at the $L_{2,3}$-Edge of the XAS of Transition-Metal Complexes.

no. of 3d electrons, N	initial configuration, $2p^63d^N$	final configuration, $2p^53d^{N+1}$
0	1	60
1	10	270
2	45	720
3	120	1260
4	210	1512
5	252	1260
6	210	720
7	120	270
8	45	60
9	10	6

$F^0_{2p,3d}$ can also be computed, but more commonly they are calculated from other parameters corresponding to average energies of the initial and the final states, according to expressions in eqs 12 and 13. The Slater integrals are defined (in hartrees) as follows:[1,3]

$$F^k_{3d,3d} = \langle R_{3d}(r_1)R_{3d}(r_2)|\frac{r_<^k}{r_>^{k+1}}|R_{3d}(r_1)R_{3d}(r_2)\rangle \quad k = 0, 2, 4 \tag{14}$$

$$F^k_{2p,3d} = \langle R_{2p}(r_1)R_{3d}(r_2)|\frac{r_<^k}{r_>^{k+1}}|R_{2p}(r_1)R_{3d}(r_2)\rangle \quad k = 0, 2 \tag{15}$$

$$G^k_{2p,3d} = \langle R_{2p}(r_1)R_{3d}(r_2)|\frac{r_<^k}{r_>^{k+1}}|R_{3d}(r_1)R_{2p}(r_2)\rangle \quad k = 1, 3 \tag{16}$$

Moreover, for the crystal-field interaction, using a 3d radial function and a simple point-charge model, the following radial integrals can be calculated for octahedral, tetragonally distorted, and/or square-planar metallic sites (expressed in hartrees)

$$10D_q = \frac{10}{6}z\langle R_{3d}(r)|\frac{r^4}{a^5}|R_{3d}(r)\rangle \tag{17}$$

$$D_s = \frac{2}{7}\left(z_a\langle R_{3d}(r)|\frac{r^2}{a^3}|R_{3d}(r)\rangle - z_b\langle R_{3d}(r)|\frac{r^2}{b^3}|R_{3d}(r)\rangle\right) \tag{18}$$

$$D_t = \frac{2}{21}\left(z_a\langle R_{3d}(r)|\frac{r^4}{a^5}|R_{3d}(r)\rangle - z_b\langle R_{3d}(r)|\frac{r^4}{b^5}|R_{3d}(r)\rangle\right) \tag{19}$$

where r represents the distance of a metal 3d electron with respect to its nucleus, a represents the distance of the point charges (representing the ligands) with respect to the position of the metal nucleus (within an octahedral site) and also represents the distance of the ligands in the xy plane (with respect to the metal nucleus) in a tetragonally distorted octahedral or a square planar complex. Finally, b represents the distance of the ligands in the z axis of a tetragonally distorted octahedral complex.

In this work, we consider the direct optimization of Slater parameters, $F^k_{3d,3d}$, $F^k_{2p,3d}$, and $G^k_{2p,3d}$ (scaled from Hartree–Fock values), and of crystal field parameters $10D_q$, D_s, and D_t as empirical parameters. However, this methodology can be also extended to optimize instead the underlying radial functions 2p and 3d, metal–ligand bond distances, and charge of the ligands (a, b, z_a and z_b in eqs 17 and 18). For example, if hydrogen-like radial functions were to be used with

$$R_{3d} = \frac{\sqrt{8}}{27\sqrt{5}}\left(\frac{\zeta_{3d}}{3a_0}\right)^{3/2}\left(\frac{\zeta_{3d}r}{a_0}\right)^2 e^{-\zeta_{3d}r/3a_0} \tag{20}$$

and

$$R_{2p} = \frac{1}{\sqrt{3}}\left(\frac{\zeta_{2p}}{2a_0}\right)^{3/2}\left(\frac{\zeta_{2p}r}{a_0}\right)e^{-\zeta_{2p}r/2a_0} \tag{21}$$

the effective "nuclear charge", ζ_{3d}, can be set up as one of the grid parameters with the option of also including ζ_{2p}. This approach is utilized here to model the $L_{2,3}$-edge XAS spectrum of Mn_2O_3, specifically to account for the crystal field in the highly distorted Mn^{3+} sites, as discussed below.

Calculation of $L_{2,3}$-Edge XAS Spectra. The $L_{2,3}$-edge XAS spectra are calculated according to the Fermi golden rule

$$I(h\nu) \propto \sum_f |\langle\Psi_f|\hat{T}|\Psi_i\rangle|^2\delta(E_f - E_i - h\nu) \tag{22}$$

where, $h\nu$ is the energy of the absorbed photons, Ψ_i is the wave function of the ground state in the initial configuration $3d^N$, and E_i is the corresponding eigenvalue. Moreover, Ψ_f represents each of the states in the final configuration, $2p^53d^{N+1}$, and E_f represents the corresponding eigenvalues. Accounting for natural broadening effects, the Dirac δ function adopts the Lorentzian profile with a full-width at half-maximum (fwhm) parameter Γ_f, giving

$$I(h\nu) \propto \sum_f |\langle\Psi_f|\hat{T}|\Psi_i\rangle|^2\frac{1}{\pi}\frac{\frac{1}{2}\Gamma_f}{(E_f - E_i - h\nu)^2 + \left(\frac{1}{2}\Gamma_f\right)^2} \tag{23}$$

Additional experimental broadening is accounted for with the convolution of a Gaussian profile (given by eq 24) with the Lorentzian-broadened spectrum, according to eq 25

$$G(h\nu) = \frac{1}{\left(\frac{\Gamma_G}{\sqrt{8\ln 2}}\right)\sqrt{2\pi}}\exp\left(-\frac{(E_f - E_i - h\nu)^2}{2\left(\frac{\Gamma_G}{\sqrt{8\ln 2}}\right)^2}\right) \tag{24}$$

$$V(h\nu) = \int_{-\infty}^{\infty} G(h\nu')L(h\nu - h\nu')\,\mathrm{d}(h\nu') \tag{25}$$

where the standard deviation (σ) in the Gaussian profile is related to the fwhm parameter Γ_G according to $\Gamma_G = \sqrt{8\ln 2}\,\sigma$. Moreover, the Voigt profile from eq 25 implies that every point within a Lorentzian profile and a natural broadening Γ_L is broadened using a Gaussian profile with experimental broadening Γ_G so that the intensity of the Lorentzian point is distributed according to the Gaussian profile, centered around the Lorentzian point with broadening Γ_G. An alternative to the Voigt profile is the pseudo-Voigt profile, in which a single broadening parameter (Γ_f) accounts for both sources of broadening (natural and experimental) and is related to the final state of the transition). In this profile the line shape is defined by the parameter η, according to eq 26.

$$V(h\nu, \Gamma_f, \eta) = (1 - \eta)L(h\nu, \Gamma_f) + \eta G(h\nu, \Gamma_f) \tag{26}$$

Thus, when $\eta = 0$, the pseudo-Voigt profile is fully Lorentzian and when $\eta = 1$ the line shape is fully Gaussian.

Figure S1a shows the Lorentzian and Gaussian profiles compared to a pseudo-Voigt profile with $\eta = 0.5$. Moreover, Figure S1b shows three hypothetical spectral lines broadened with two different values of Γ (fwhm) using the pseudo-Voigt profile with $\eta = 0.2$. The areas under the curves in all cases are equal to the intensities of the spectral lines. In this work, we use the pseudo-Voigt profile to broaden the calculated spectral lines to produce each simulation. In this sense, the Lorentzian broadening of this lines and the parameter η are both optimized and set as free-floating parameters. For this, the broadening parameter Γ_{L_3} for all lines at the L_3-edge are set up to be all the same. A different parameter Γ_{L_2} is used for all lines at the L_2-edge, due to Coster–Kronig Auger transitions (as additional paths for relaxation in the final state of L_2 states, compared to L_3, which alters their core-hole lifetimes[42]). To calculate the XAS spectra within the dipole approximation, the transition operator $\hat{T}$ is expanded in terms of the weighted normalized spherical harmonics C_1^{-1}, C_1^0, and C_1^{+1} with

https://doi.org/10.1021/acs.inorgchem.2c02830
Inorg. Chem. 2023, 62, 3738−3760

$$\hat{T} = \left(\frac{1+i}{\sqrt{2}}\right)C_1^{-1} + \left(\frac{i-1}{\sqrt{2}}\right)C_1^{1} + C_1^{0} \tag{27}$$

from which we calculate a density matrix **T**. This relates each microstate in the initial configuration $3d^N$ with each microstate in the final configuration $2p^5 3d^{N+1}$ through the electric dipole transition operator $\hat{T}$. This matrix is unique and unchanged for a given $3d^N$ configuration and thus calculated once and also stored. Then, the strengths of the transition lines are calculated from it using the expressionwhere vector $\mathbf{\Psi}_i$ represents the ground state expressed as a

$$\mathbf{S}^{1/2} = \mathbf{\Psi}_i^{\dagger} \cdot \mathbf{T} \cdot \mathbf{\Psi}_f \tag{28}$$

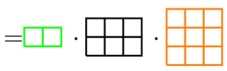

linear combination of microstates in the initial configuration $3d^N$ and $\mathbf{\Psi}_f$ is a matrix whose columns represent the states in the final configuration $2p^5 3d^{N+1}$, each expressed as a linear combination of microstates in the final configuration. Thus, vector **S** contains the line strengths which the code broadens using the pseduo-Voigt profile, as given by eq 26. Effects of temperature are considered by calculating line strengths from additional states Ψ_i in the initial configuration, $3d^N$, using a Boltzmann factor (f_{B_i}) given by

$$f_{B_i} = \exp\left(-\frac{E_i - E_0}{k_B T}\right) \tag{29}$$

where E_0 represents the energy of the ground-state multiplet in the initial configuration.

Edge Jumps. In order to reproduce all the spectral features in the experimental data discussed here, it is necessary to fit the L_3- and L_2-edge jumps together with the crystal field multiplet simulations as part of the physical model. The edge jump can be envisaged as a continuum of electronic transitions ocurring from 2p levels to the continuum where the ionized electrons would possess increasing kinetic energies. Assuming then a pseudo-Voigt profile for each of this continuum of transitions, the result is the cumulative pseudo-Voigt function given by

$$\mathrm{edge}(h\nu, \Gamma_f, \eta) = (1-\eta)\left(\frac{1}{\pi}\arctan\left(\frac{h\nu - E_I}{\frac{\Gamma_f}{2}}\right) + \frac{1}{2}\right) + \frac{\eta}{2}\left(1 + \mathrm{erf}\left(\frac{(h\nu - E_I)\sqrt{4\ln 2}}{\Gamma_f}\right)\right) \tag{30}$$

where E_I is the inflection point of the edge jump which is related to the ionization process of a 2p electron. In the case of $L_{2,3}$-edge XAS, two edge jumps often appear within the range of energy considered. This is due to a large 2p spin−orbit coupling in the final state, which implies the generation of states $2p_{3/2}$ and $2p_{1/2}$ after removing a 2p electron. As these two states are split by $3/2\xi_{2p}$, the two edge jumps should have inflection points E_I and $E_I + 3/2\xi_{2p}$, respectively, for the states $2p_{3/2}$ and $2p_{1/2}$, as shown in Figure 1. Moreover, the intensity ratio between both edges $(I_{L_3}: I_{L_2})$ is expected to be 2:1, evaluated from the ratio of multiplicities between the $2p_{3/2}$ and $2p_{1/2}$ states. Ideally, the inclusion of these two edge jumps should contemplate also the inclusion of a background function which slightly changes its steepness after each of the edge jumps. However, very often the background is removed as part of the initial reduction of the raw data. Consequently, this could cause the intensity ratio during the fitting procedure to not correspond exactly to the expected 2:1 ratio. In this case, as we digitized the experimental data from previous studies where the experimental data presented has been reduced (with the background removed), we allowed the intensity ratio to be a floating parameter to be fit along with the crystal field multiplet simulations. We highlight here that this holistic approach of fitting the edge jumps together with the simulations is useful to define the inflection points

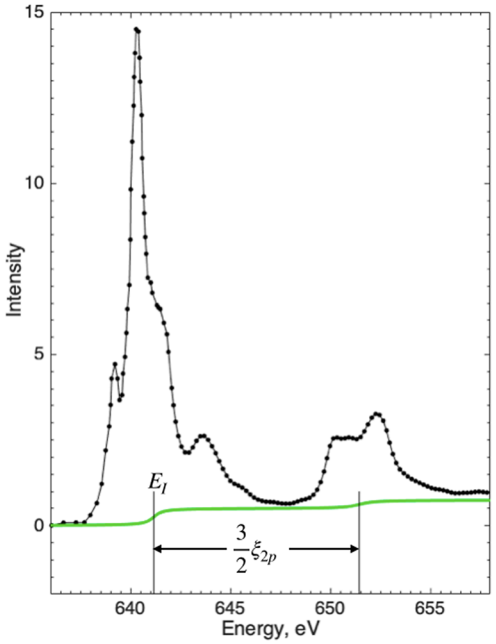

Figure 1. L_3- and L_2-edge jump functions as part of the physical model of MnO. Together with crystal field multiplet simulations, these edge jump functions are used to fit the multiplet simulations to the experimental Mn $L_{2,3}$-edge XAS of MnO. A similar model is used here for the analysis of the corresponding $L_{2,3}$-edge XAS spectra of CaO, CaF_2 $LiMnO_2$, and Mn_2O_3.

of the edge jumps corresponding to ionization energies which are often correlated to oxidation states in the K-edge XAS analysis. However, one important consideration from empirical observations is that one should expect the two edge jumps to be positioned near the corresponding bound transitions only if the material is considered a good electricity conductor or if the compound involved is a molecular species. On the other hand, if the material is a semiconductor or an insulator, the position of the edge jumps can move significantly at higher energies, to the point in which the L_3-edge jump could be visible at energies where the L_2-bound transitions start to appear. Consequently, the second edge jump would only be visible if enough data are collected beyond the point at which bound transitions for the L_2-edge are visible. Thus, the correlations of energy positions of the edges to effective nuclear charge (and oxidation state) in the $L_{2,3}$-edge are not as straightforward as in the case of the K-edge XAS analysis, unless molecular species with similar structures are being compared. The same would be true when comparing results for materials with similar ligands and conducting properties. Herein, the fit models for the experimental data sets included only the crystal field simulations and the edge jump functions, as shown in Figure 1.

The Adaptive Grid Algorithm. We have implemented in Matlab a crystal-field multiplet model to simulate X-ray absorption spectra at the $L_{2,3}$-edge of transition-metal complexes (that is, for the excitation of a 2p electron in the metal to empty molecular orbitals with metal-3d character). All operators for electron−electron, spin−orbit coupling, and crystal field are represented with a matrix spanning through a base of microstates whose size depends on the $3d^N$ configuration. Then, the magnitude of each interaction is amplified by radial parameters that can be adjusted to fit the experimental data, where radial integrals, as given by eqs 14−19, are treated as empirical parameters. Traditionally, these are manually adjusted until the simulation fits the experimental data. In the case of electron−electron repulsion parameters (Slater integrals), the values obtained from Hartree−Fock calculations (performed with the code developed by Cowan[3]), are scaled down to about 80% to properly represent atomic values.[1,43] Then, they are scaled down further because of covalency. In the case of parameters $10D_q$, D_s, and D_t, as defined by eqs 17−19, they

https://doi.org/10.1021/acs.inorgchem.2c02830
Inorg. Chem. 2023, 62, 3738−3760

are directly adjusted until the simulation fits the experiment. This process could be very cumbersome, and some have even suggested that finding a solution does not necessarily guarantee a single solution. In this regard, we have made significant advances toward a methodology that explores a large solution space for these parameters and automatically finds good fits. For metal $L_{2,3}$-edge XAS, our code has been wrapped up as a function of BlueprintXAS[9] so that we can optimize simulation parameters effecting Hamiltonians in addition to free-floating parameters such as scaling factors, global energy shifts, and Lorentzian (natural) and Gaussian (experimental) broadening parameters. Every transition is modeled as a pseudo-Voigt with a common half-width at half-maximum parameter (referred here further as hwhm) and a shape-related parameter (η) which weights-in the Gaussian profile. For every combination of radial integral parameters, free-floating parameters are optimized using a trust-region nonlinear least-squares algorithm. BlueprintXAS is a Matlab-based optimizer originally developed to analyze X-ray spectra using empirical peaks, but with the advantage of obtaining multiple solutions in nonlinear optimizations in order to explore large solution space regions, to reduce user bias in the definition of the start point and to estimate uncertainties for each parameter.[9,10] In this work, BlueprintXAS expands its capabilities to work in conjunction with an adaptive grid algorithm, through its grid mode. In this mode, while the optimization of parameters such as composition, scaling factors, broadening parameters, and energy shifts are treated in the same way as in the fit mode (the regular mode of BlueprintXAS), the nonadjustable parameters by the trust-region algorithm are optimized by creating a grid. Radial parameters as inputs of the multiplet simulations have an effect on Hamiltonians and thus need to be defined as grid parameters for which their optimization involves defining lower and upper bounds and a given step size (precision) to generate a number of points for each grid parameter. A mesh from the combination of all points for every parameter is then obtained. If the step size is too small, the number of points in the final grid is extremely large, so much so that trying simulations of every point in the grid will require months in some cases. Thus, we developed an adaptive grid algorithm, which always starts with wider ranges for every parameter and relatively large step sizes so that the final number of points in the grid is reasonable (below 50000 points takes only a few days to solve). Thus, after a first cycle, the program selects the best fits from which, using the average and two standard deviations for every parameter, it recalculates the lower and upper limits of the simulation parameters. This increases the precision of the step size while maintaining the same number of points in the final grid. The selection of good fits is based on the sum of squared errors (SSE), defined as

$$\mathrm{SSE} = \sum_i (y_i - f_i)^2 \tag{31}$$

where y_i represents a data point in the XAS spectrum and f_i represents a corresponding prediction from the model which includes the crystal field multiplet simulation. Moreover, the total number of best fits is selected by the user, but importantly, in order for the algorithm to identify good regions within the solution space, the number of good fits should be a fraction of the number of points in the grid. In this case, the number of fits selected is set to be no more than 5% for the examples presented in this study. Thus, the calculation of new limits and step sizes for the grid in subsequent cycles is based on the average and two standard deviations of the fit parameters within the selected best fits. As this adaptive grid algorithm moves forward, the step sizes in each of the radial parameters included in the grid become refined and the lower and upper bounds are recalculated to obtain grids of the same size in subsequent cycles. In this study we use 4 cycles for the fitting of calculated spectra and 5 cycles for the fitting of all the experimental data. As an example, consider Figure 2, which shows the evolving adaptive grid created from parameters $10D_q$ and D_s, as were used in the case of $LiMnO_2$. In cycle 1, the original grid is formed from the lower and upper limits of these parameters with a $10D_q$ value ranging from 1.7 to 2.5 eV in steps of 0.1 eV (9 points) and with values of D_s ranging from 0.2 to 0.5 eV in steps of 0.1 eV (4 points). Thus, the size of the grid for these two parameters is 9 × 4 = 36

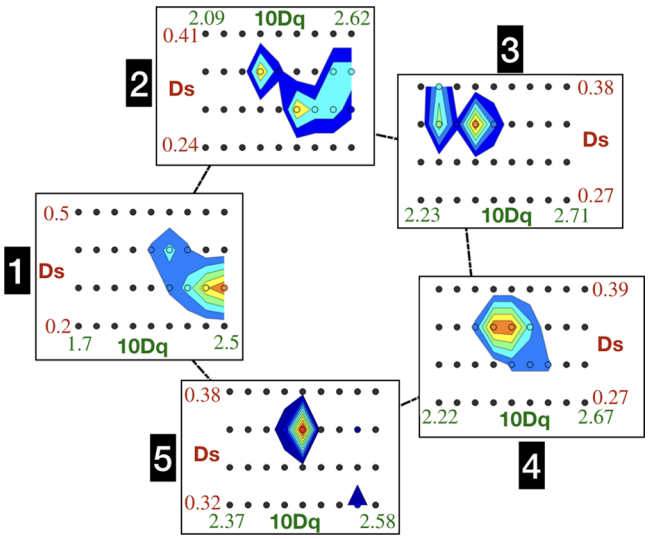

Figure 2. Adaptive grid algorithm showing 5 cycles of refinement, as implemented in BlueprintXAS for the optimization of the crystal field simulation to the experimental Mn L-egde XAS data of $LiMnO_2$. The step size for the values of the parameters $10D_q$ and D_s gets refined after every cycle, according to the regions with the smallest value of sum of squared errors (SSE) between simulation and experimental data. The grid shown in this figure is a partial representation of a much larger grid from the five parameters listed in Table 4 for $LiMnO_2$. The contour plots shown in each cycle are not representations of errors but instead representations of where the best fits are located (based on their SSE value).

points. Then, after going through every point of the grid and optimizing the free-floating parameters in the simulation, the best fits are identified (shaded regions in Figure 2). From there, a new grid with the same 36 points is generated but with a more precise step size for each of the parameters. This process continues for a total of 5 cycles. Importantly, the grid shown in Figure 2 for $LiMnO_2$ is not a complete representation, as it only shows a map of the solution space for two of the five parameters. The complete grid parameters for this compound are given in Table 4. The contour plots in Figure 2 within the grid of each cycle are not representations of errors but instead representations of where the best fits are located. In this sense, the results discussed in the next sections are then a representation of the local sensitivity based on the best fits rather than reflecting uncertainties or confidence levels within a single global fit.

In this study, we use the adaptive grid algorithm to fit crystal field multiplet simulations to find radial and free-floating parameters that best fit the calculated XAS $L_{2,3}$-edge based on known parameters for a series of d^0−d^7 systems. These systems are based on Ti, V, Cr, Fe, and Co in different symmetrical environments. Moreover, we use this methodology to fit crystal field multiplet simulations to experimental $L_{2,3}$-edge XAS data for a series of previously published Ca and Mn complexes. In the case of the Mn $L_{2,3}$-edge XAS data, the fit model included cumulative pseudo-Voigt functions to model the L_3- and L_2-edge jumps, as discussed in the previous section. The next sections discuss each of the data sets considered in this work, while Tables 3 and 4 give the lower and upper limits and the step size for each of the parameters used in the fitting of all data sets considered in this work. The size of the grid derived from the number of points for each of these parameters is also given. Keeping in mind that one crystal field simulation using our code takes less than 1 s, while the follow-up optimization of the free-floating parameters such as scaling factors, broadening, and energy shifts takes on average 10 s using a trust-region nonlinear fitting algorithm, completing a job with the adaptive grid algorithm for a calculation with a grid size of 1000 points would take 1000 points/cycle × 10 s/point × 5 cycles = 50000 s or ∼14 h. A quick tutorial of how to run these types of calculations in BlueprintXAS is provided in section S10 of the Supporting

https://doi.org/10.1021/acs.inorgchem.2c02830
Inorg. Chem. 2023, 62, 3738−3760

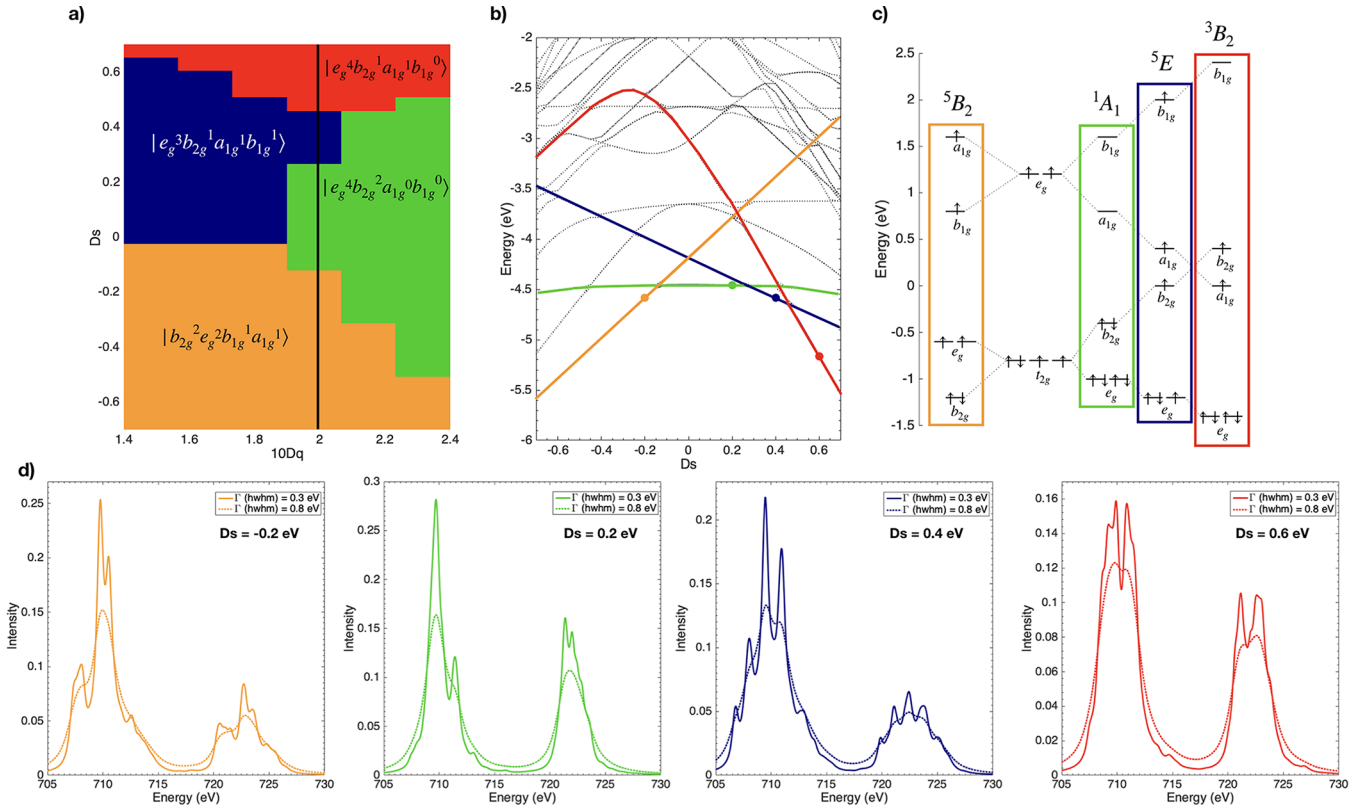

Figure 3. (a) Phase diagram for Fe^{2+} complexes in D_{4h} symmetry identifying regions of $10D_q$ and D_s where the ground state is $^5B_2$, $^1A_1$, ^5E, and $^3B_2$. (b) Tanabe−Sugano diagram showing the energy of the multiplets for different values of D_s at a fixed value of $10D_q$ = 2.0 eV, where all 4 states in the phase diagram in (a) are present. (c) Crystal field diagrams for the states highlighted with points in (b). (d) Corresponding $L_{2,3}$-edge XAS calculated from the identified ground states depicted in (c). The selected set of parameters used to create the data sets in (d) are given in Table S3. Continuous lines represent the spectra broadened with a hwhm parameter of 0.3 eV, while dashed lines represent spectra broadened with a hwhm of 0.8 eV.

Information, where additional recommendations are made for large grid sizes (with a large number of parameters and/or for cases in which several components are involved.)

Calculated Data Sets. To test how effective and robust the adaptive grid algorithm is in finding the solution for the radial and free-floating parameters, a series of calculated data sets have been created from known parameters based on d^0−d^7 systems of Ti, V, Cr, Fe, and Co in different symmetry environments. Each data set was broadened using two different values of hwhm, 0.3 and 0.8 eV, all with Lorentzian line shapes. All calculated data sets were created assuming a temperature of 10 K. In the case of d^0 systems, Ti^{4+} is considered in three different environments: (a) as a free ion, (b) in a nearly octahedral environment (such as in the case of $FeTiO_3$, and (c) in a distorted-octahedral environment, such as in the case of TiO_2. The crystal-field parameters used to create these data sets are given in Table S3. Additional data sets for d^1−d^4 systems based on the ions V^{3+}, V^{4+}, Cr^{2+} and Cr^{3+} were all created in an octahedral environment with a value of $10D_q$ = 1.5 eV and reduction factors for $\alpha(F^k_{3d,3d})$ and $\beta(F^k_{2p,3d})$, $\beta(G^k_{2p,3d})$ equivalent to 80% with respect to Hartree−Fock values. All created spectra in the series d^0−d^4 shown in Figure S2 display the same features reproduced before in previous studies for the same parameters. For simplicity, in all these series the 3d spin−orbit coupling parameter (ξ_{3d}) is set to zero.

Furthermore, a Tanabe−Sugano diagram of Fe^{2+} computed with $\alpha(F^k_{3d,3d})$ = 80% (from the Hartree−Fock values) and with ξ_{3d} set to zero reveals a high-spin (HS) ground state ($^5T_2$) at $10D_q$ values below ca. 1.8 eV and a low-spin (LS) ground state ($^1A_1$) above this value (see Figure S3). Thus, we calculated data sets for Fe^{2+} octahedral complexes with $10D_q$ values of 1.0 and 3.0 which originate from well-established ground states. Table S3 gives the parameters utilized for these calculations. We then calculated a phase diagram using CTM4DOC[44] to identify different ground states in Fe^{2+}-D_{4h}

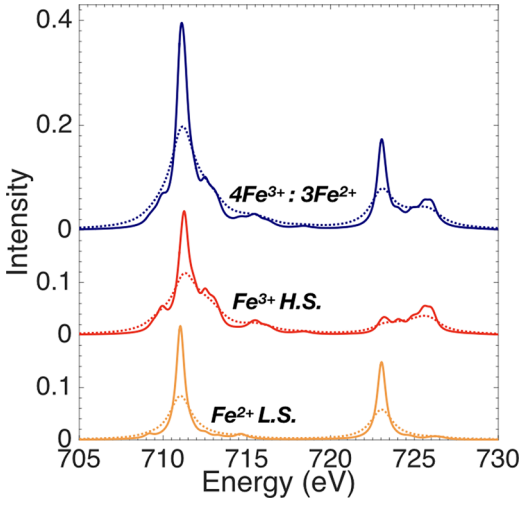

Figure 4. Calculated data sets for the $L_{2,3}$-edge XAS of a mixed valence complex inspired by Prussian blue (top), showing the contribution from the Fe^{3+} sites with a high-spin ground state (center) and and the contribution from the Fe^{2+} sites in a low-spin state (bottom). The parameters used for the Fe^{3+} and Fe^{2+} sites are given in Table S3. The scaling factors used for each site correspond to a stoichometric ratio of Fe^{3+}:Fe^{2+} = 4:3. Continuous lines represent the spectra broadened with a hwhm parameter of 0.3 eV, while dashed lines represent spectra broadened with a hwhm of 0.8 eV.

https://doi.org/10.1021/acs.inorgchem.2c02830
Inorg. Chem. 2023, 62, 3738−3760

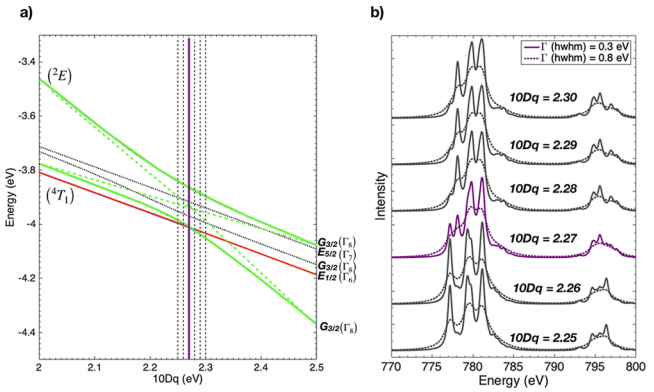

Figure 5. (a) Tanabe–Sugano diagram for Co^{2+} within an energy range near a spin-crossover transition point. The reduction parameter $\alpha(F^k_{3d,3d})$ and the reduction of the 3d spin–orbit coupling are maintained at 80% with respect to the Hartree–Fock values, while the value of $10D_q$ is increased from 2.0 to 2.5 eV. Below a value of $10D_q$ = 2.27 eV, the ground state is $E_{1/2}$ ($^4T_1$). And for a value of $10D_q$ greater than 2.27 eV, the ground state is $G_{3/2}$ (^2E + $^4T_1$), resulting from the mixing through the 3d spin–orbit operator. Exactly at $10D_q$ = 2.27 eV, however, the ground state is a mixture of states, as indicated in Table 2. (b) $L_{2,3}$-edge XAS of octahedral Co^{2+} complexes reproduced with the same $10D_q$ value as in the vertical lines of the Tanabe–Sugano shown in (a). The spectrum obtained with $10D_q$ = 2.27 was used to test the grid algorithm, using two different Lorentzian broandenings. Continuous lines represent the spectra broadened with a hwhm parameter of 0.3 eV, while dashed lines represent spectra broadened with a hwhm of 0.8 eV.

complexes by varying the value of $10D_q$ and D_s while maintaining the values of $\alpha(F^k_{3d,3d})$ at 80% (from Hartree–Fock values) and with D_t and ξ_{3d} set to zero. As shown in Figure 3a, there are 4 different ground states within the explored region, including two different high-spin states ($^5B_2$ and ^5E), one low-spin state ($^1A_1$), and one intermediate-spin state ($^3B_2$). At $10D_q$ = 2.0 eV, all four could be stabilized with different values of D_s, as indicated in Figure 3b. Thus, we calculated the $L_{2,3}$-edge XAS of Fe^{2+} starting from each of the ground states highlighted in Figure 3c (with values of D_s = −0.2, 0.2, 0.4 and 0.6 eV), obtaining the spectra shown in Figure 3d. Table S3 gives the parameters utilized to calculate the corresponding $L_{2,3}$-edge XAS spectra. Like in the case of d^0–d^4 systems, in each of the Fe^{2+} cases (O_h and D_{4h}), we calculated a narrowed data set with hwhm = 0.3 eV and a broadened data set with hwhm = 0.8 eV, using Lorentzian line shapes.

Then, to increase the challenge for the adaptive grid algorithm, we also calculated data sets for a complex or composite material inspired by Prussian blue. In this case, the calculated Fe $L_{2,3}$-edge XAS corresponds to a mixture of Fe^{3+} and Fe^{2+} sites, both in an octahedral environment. The Fe^{3+} contribution was calculated from a value of $10D_q$ = 1.0 eV, whereas the Fe^{2+} contribution was calculated using a value of $10D_q$ = 4.0 eV. In both cases, the reduction of Slater integrals was set to 80% with respect to Hartree–Fock values and the value of the 3d spin–orbit coupling was set to zero. Moreover, to account for the same $4Fe^{3+}$:$3Fe^{2+}$ stoichometric ratio as in Prussian blue, the calculated spectra for Fe^{3+}, whose intrinsic intensity accounts for five 3d holes, was multiplied by a factor of 1, while the corresponding spectra of Fe^{2+}, whose intrinsic intensity accounts for four 3d holes, was multiplied by a factor of 4/3. The resulting data sets (calculated with a hwhm of 0.3 and 0.8 eV) as well as the contributing components are shown in Figure 4. In the fitting procedure of these data sets, in addition to optimizing the crystal field and the reduction of Slater integrals for each Fe site (setting these as grid parameters), the Lorentzian broadening (hwhm) and the composition (or intensity ratio between the two sites) were also fit.

Table 2. Composition of the First Five Low-Lying Multiplets in the Ground-State Configuration (d^7) of Co^{2+}, Calculated with a Reduction in the Slater Integrals and Spin–Orbit Coupling Equivalent to 80% of Their Hartree–Fock Values, at Three Different Values of $10D_q$: (a) Below the Spin-Crossover Transition Point ($10D_q$ = 2.25 eV); (b) Exactly at the Spin-Crossover Transition Point ($10D_q$ = 2.27 eV); (c) Above the Spin-Crossover Transition Point ($10D_q$ = 2.30 eV).

energy (eV)	multiplicity	O' term	cubic term	O_h crystal field configuration
		(a) $10D_q$ = 2.25 eV		
−3.997	2	$\Gamma_6(E_{1/2})$	$^4T_1$ 100%	$\|t_{2g}^5e_g^2\rangle$ 95.5%
				$\|t_{2g}^4e_g^3\rangle$ 4.5%
−3.987	4	$\Gamma_8(G_{3/2})$	$^4T_1$ 58.4%	$\|t_{2g}^5e_g^2\rangle$ 55.4%
			^2E 41.6%	$\|t_{2g}^6e_g^1\rangle$ 41.6%
				$\|t_{2g}^4e_g^3\rangle$ 3.0%
−3.952	4	$\Gamma_8(G_{3/2})$	$^4T_1$ 87.5%	$\|t_{2g}^5e_g^2\rangle$ 83.9%
			^2E 12.2%	$\|t_{2g}^6e_g^1\rangle$ 12.2%
				$\|t_{2g}^4e_g^3\rangle$ 3.9%
−3.901	2	$\Gamma_7(E_{5/2})$	$^4T_1$ 100%	$\|t_{2g}^5e_g^2\rangle$ 95.9%
				$\|t_{2g}^4e_g^3\rangle$ 4.1%
−3.842	4	$\Gamma_8(G_{3/2})$	$^4T_1$ 53.8%	$\|t_{2g}^5e_g^2\rangle$ 51.6%
			^2E 46.2%	$\|t_{2g}^6e_g^1\rangle$ 44.7%
				$\|t_{2g}^4e_g^3\rangle$ 3.3%
		(b) $10D_q$ = 2.27 eV		
−4.012	4 + 2	$\Gamma_8(G_{3/2})$ + $\Gamma_6(E_{1/2})$	$^4T_1$ 66.0%	$\|t_{2g}^5e_g^2\rangle$ 62.9%
			^2E 34.0%	$\|t_{2g}^6e_g^1\rangle$ 34.0%
				$\|t_{2g}^4e_g^3\rangle$ 3.1%
−3.969	4	$\Gamma_8(G_{3/2})$	$^4T_1$ 91.3%	$\|t_{2g}^5e_g^2\rangle$ 87.6%
			^2E 8.7%	$\|t_{2g}^6e_g^1\rangle$ 8.7%
				$\|t_{2g}^4e_g^3\rangle$ 3.7%
−3.916	2	$\Gamma_7(E_{5/2})$	$^4T_1$ 100%	$\|t_{2g}^5e_g^2\rangle$ 95.9%
				$\|t_{2g}^4e_g^3\rangle$ 4.1%
−3.865	4	$\Gamma_8(G_{3/2})$	$^4T_1$ 61.0%	$\|t_{2g}^5e_g^2\rangle$ 58.4%
			^2E 39.0%	$\|t_{2g}^6e_g^1\rangle$ 37.9%
				$\|t_{2g}^4e_g^3\rangle$ 3.7%
		(c) $10D_q$ = 2.30 eV		
−4.052	4	$\Gamma_8(G_{3/2})$	^2E 65.0%	$\|t_{2g}^6e_g^1\rangle$ 65.0%
			$^4T_1$ 35.0%	$\|t_{2g}^5e_g^2\rangle$ 33.1%
				$\|t_{2g}^4e_g^3\rangle$ 1.9%
−4.034	2	$\Gamma_6(E_{1/2})$	$^4T_1$ 100%	$\|t_{2g}^5e_g^2\rangle$ 95.5%
				$\|t_{2g}^4e_g^3\rangle$ 4.5%
−3.994	4	$\Gamma_8(G_{3/2})$	$^4T_1$ 94.5%	$\|t_{2g}^5e_g^2\rangle$ 90.5%
			^2E 5.5%	$\|t_{2g}^6e_g^1\rangle$ 5.5%
				$\|t_{2g}^4e_g^3\rangle$ 4.0%
−3.939	2	$\Gamma_7(E_{5/2})$	$^4T_1$ 100%	$\|t_{2g}^5e_g^2\rangle$ 96.0%
				$\|t_{2g}^4e_g^3\rangle$ 4.0%
−3.898	4	$\Gamma_8(G_{3/2})$	$^4T_1$ 70.2%	$\|t_{2g}^5e_g^2\rangle$ 67.9%
			^2E 29.8%	$\|t_{2g}^6e_g^1\rangle$ 29.8%
				$\|t_{2g}^4e_g^3\rangle$ 2.3%

Finally, we created data sets based on Co^{2+}, from which the ground state is a mixture of high- and low-spin states enabled by the 3d spin–orbit coupling interaction. In the absence of 3d spin–orbit coupling, the low-spin (^2E) and the high-spin ($^4T_1$) states states cannot mix. However, once the 3d spin–orbit coupling of Co^{2+} is put on, the direct product of the spin and orbital components in the $^4T_1$ state yields 4 states

$$\Gamma_8(G_{3/2}) \otimes \Gamma_4(T_1) = \Gamma_6(E_{1/2}) \oplus \Gamma_7(E_{5/2}) \oplus 2\Gamma_8(G_{3/2}) \quad (32)$$

https://doi.org/10.1021/acs.inorgchem.2c02830
Inorg. Chem. 2023, 62, 3738–3760

Table 3. Grid Parameters, Their Initial Lower and Upper Limits, and Their Initial Step Sizes for the Fitting of All the Calculated Data Sets Discussed in the Text[a]

	Ti^{4+} systems								
	atomic			O_h			D_{4h}		
parameter	lower	upper	step	lower	upper	step	lower	upper	step
$10D_q$	0.0	2.4	0.2	0.0	2.4	0.2	0.0	2.4	0.1
D_s	−0.20	0.20	0.05	−0.20	0.20	0.05	−0.20	0.20	0.05
D_t	−0.10	0.10	0.02	−0.10	0.10	0.02	−0.10	0.10	0.02
$\beta(F^k_{2p,3d},G^k_{2p,3d})$, %	48	96	8	48	96	8	48	96	8
	grid size: 9009			grid size: 9009			grid size: 9009		
	d^1−d^4 systems			Fe^{2+}-O_h (HS, LS) and D_{4h} ($^5B_2$, $^1A_1$, ^5E, $^3B_2$)			Co^{2+}-O_h (mixed spin)		
parameter	lower	upper	step	lower	upper	step	lower	upper	step
$10D_q$	0.0	2.5	0.1	0.5	3.5	0.1	1.6	3.0	0.2
D_s		fixed at zero		−0.70	0.70	0.05		fixed at zero	
D_t		fixed at zero		−0.20	0.20	0.04		fixed at zero	
$\alpha(F^k_{3d,3d})$, %	48	100	4		fixed at 80%		64	96	4
$\beta(F^k_{2p,3d}, G^k_{2p,3d})$, %	48	100	4		fixed at 80%		64	96	4
Red(ζ_{3d}), %		fixed at zero			fixed at zero		0	100	20
	grid size: 5096			grid size: 9889			grid size: 3888		
	$4Fe^{3+}$ (HS):$3Fe^{2+}$ (LS) system								
	Fe^{3+}			Fe^{2+}					
parameter	lower	upper	step	lower	upper	step			
$10D_q$	1.0	5.0	0.5	1.0	5.0	0.5			
$\alpha(F^k_{3d,3d}, F^k_{2p,3d}, G^k_{2p,3d})$,[b] %	64	96	8	64	96	8			
	grid size: 2025								

[a]The total grid size in each case is also provided. The values for reduction parameters $\alpha(F^k_{3d,3d})$ and $\beta(F^k_{2p,3d}, G^k_{2p,3d})$ given here correspond to the reduction from Hartree−Fock values. [b]For the $4Fe^{3+}$: $3Fe^{2+}$ system, a single parameter per site was set to collectively reduce all of the Slater integrals ($F^k_{3d,3d}$, $F^k_{2p,3d}$, and $G^k_{2p,3d}$).

while the direct product of the spin and orbital components in the ^2E state gives a single state

$$\Gamma_6(E_{3/2}) \otimes \Gamma_3(E) = \Gamma_8(G_{3/2}) \quad (33)$$

(For the convenience of the reader, a character table for the O' double group and a derived table for direct products in this double group are provided in Tables S1 and S2.) This means that the $G_{3/2}$ state in the low-spin ^2E state is allowed to mix with two of the states in the high-spin $^4T_1$ state. To chose the right value of $10D_q$ at which the spin crossover occurs, a Tanabe−Sugano diagram is calculated near this region using 80% for the reduction of Slater integrals and for the 3d spin−orbit coupling of Co^{2+} (with respect to Hartree−Fock values). As shown in Figure 5, it is necessary to set the value of $10D_q$ to 2.27 eV in order to have a calculation which reflects contributions from both states. This is also evident from the composition listed in Table 2 for the first 5 low-lying multiplets in the ground-state configuration d^7. Thus, fitting the data sets created with a $10D_q$ of 2.27 represents the most challenging case, as it requires finding solutions with a precision of two decimal significant figures. Table S3 gives the parameters used to create the Co^{2+} data sets discussed in this section.

In summary, to test the adaptive grid algorithm, crystal field multiplet simulations were fit for all data sets calculated and are shown in Figures S2 and S3 and Figures 3 and 4 and in the case of Co^{2+} for the data sets shown in Figure 5 and calculated with a value of $10D_q$ = 2.27 eV only. In all cases, an initial wide range for all radial parameters was used. All of these radial parameters optimized in each case, along with the corresponding values for their lower and upper limits and their step sizes to define the initial grids, are given in Table 3. In all cases, scaling factors and Lorentzian broadenings (hwhm) were set as free-floating parameters.

Experimental Data. We also utilized the adaptive grid algorithm to analyze previously published experimental $L_{2,3}$-edge XAS data on calcium and manganese compounds, finding new insightful information, particularly in the case of $LiMnO_2$ and Mn_2O_3. These experimental data were digitized from previous contributions[43,45] using the software webplotdigitizer. In the case of the data for Mn oxides, it was necessary to use a stretching parameter as a free-floating parameter, as the data appear to be stretched in comparison to the simulations. Figures S4−S6 show the original data for MnO, $LiMnO_2$, and Mn_2O_3 as they appeared in the original publication compared to the data after correction using a linear function that includes the stretching parameter and a global shift, both of which are part of the free-floating parameters with infinite precision. The corrected data are consistent with the spectra obtained for MnO and Mn_2O_3 from more recent studies.[46] We hypothesize that the stretching correction needed is due to early developments of sphere grating monochromators (SGM) when XAS at the $L_{2,3}$-edge of transition-metal oxides was first developed as an experimental technique. Thus, we emphasize here that, using our methodology, all the data collected in beamlines with this type of instrumentation can be corrected to account for this or similar issues related to energy calibration. To model the experimental data sets, we included cumulative pseudo-Voigt functions to account for the edge jumps in CaO, MnO, $LiMnO_2$, and Mn_2O_3, as described above. The inflection points, the line widths, the line shapes, and the intensities of these edge jumps were also fit as free-floating parameters together with the scaling factors, energy shifts, and broadening parameters for the crystal-field multiplet simulations. Table 4 gives the lower and upper limits and the step sizes for all the grid parameters used during the fitting of each experimental data set. In the case of the data for the calcium complexes, three different models were tested to find if a different scaling factor was needed for the Slater integrals $F^2_{2p,3d}$, $G^1_{2p,3d}$ and $G^3_{2p,3d}$. In the first model, all of these integrals are scaled using a single parameter. Then, in the second model, the Slater integral $F^2_{2p,3d}$ employs a different scaling factor than for $G^1_{2p,3d}$ and $G^3_{2p,3d}$. And in the

https://doi.org/10.1021/acs.inorgchem.2c02830
Inorg. Chem. 2023, 62, 3738−3760

Table 4. Grid Parameters, Their Initial Lower and Upper Limits, and Their Initial Step Sizes for the Fitting of the Experimental Data Sets Studied in This Work[a].

	CaO								
	model 1			model 2			model 3		
parameter	lower	upper	step	lower	upper	step	lower	upper	step
$10D_q$	1.30	1.60	0.05	1.30	1.60	0.05	1.30	1.60	0.05
$\beta(F^2_{2p,3d},G^1_{2p,3d},G^3_{2p,3d})$, %	72	88	2						
$\beta(F^2_{2p,3d})$, %				72	88	4	72	88	4
$\beta(G^1_{2p,3d},G^3_{2p,3d})$, %				64	96	4			
$\beta(G^1_{2p,3d})$, %							64	96	4
$\beta(G^3_{2p,3d})$, %							64	96	4
	grid size: 63			grid size: 175			grid size: 560		
	CaF_2								
	model 1			model 2			model 3		
parameter	lower	upper	step	lower	upper	step	lower	upper	step
$10D_q$	−1.00	−0.50	0.05	−0.95	−0.60	0.05	−0.95	−0.60	0.05
$\beta(F^2_{2p,3d},G^1_{2p,3d},G^3_{2p,3d})$, %	72	88	4						
$\beta(F^2_{2p,3d})$, %				72	88	4	72	88	4
$\beta(G^1_{2p,3d},G^3_{2p,3d})$, %				64	98	4			
$\beta(G^1_{2p,3d})$, %							64	98	4
$\beta(G^3_{2p,3d})$, %							64	98	4
	grid size: 55			grid size: 200			grid size: 1000		
	MnO			$LiMnO_2$			Mn_2O_3		
parameter	lower	upper	step	lower	upper	step	lower	upper	step
$10D_q$ [b]	0.88	0.96	0.02	1.70	2.50	0.1	1.0	1.6	0.1
$\alpha(F^k_{3d,3d})$, %	72.0	88.0	0.8	56	80	8	48	80	8
$\beta(F^2_{2p,3d},G^1_{2p,3d},G^3_{2p,3d})$, %	72.0	88.0	0.8	76	84	4	56	80	8
D_s				0.20	0.50	0.10			
D_t				0.06	0.18	0.04			
ζ_{3d} [c]							5.5	6.5	0.2
z [c]							1.0	1.8	0.2
	grid size: 2205			grid size: 1728			grid size: 4200		

[a]The total grid size in each case is also provided. The values for reduction parameters α and β are with respect to Hartree−Fock values. [b]In the case of Mn_2O_3 the value of $10D_q$ corresponds to the nondistorted O_h Mn^{3+} site. [c]ζ_{3d} corresponds to the effective nuclear charge of the radial function in the Mn^{3+} distorted sites, while z is the average charge of the oxygen atoms surrounding these sites.

third model, all of these integrals have their own independent scaling factor.

RESULTS AND DISCUSSION

An adaptive grid algorithm to fit crystal field multiplet simulations to $L_{2,3}$-edge XAS data has been assessed, first utilizing calculated data sets of d^0-d^7 systems in different symmetry environments and from known radial parameters to see how effectively the algorithm can find the solution. Then fitting experimental data on Ca and Mn complexes was also carried out, which included the edge jumps as part of the fit model. In the case of the calculated data sets, two different Lorentzian broadenings were fit to see how robust the algorithm is in terms of finding the right solutions in fewer resolved spectra.

Calculated Data Sets. *d^0−d^4 Systems.* Table S5 gives the results obtained for the fitting of multiplet simulations to the calculated data sets of d^0−d^4 systems. As shown in Figures S7−S9, the adaptive grid algorithm developed in this work finds the parameters of these systems remarkably well and it appears also that the solution becomes even less disperse as more features appear in the spectra on going from d^0 to d^4, regardless if the spectra are broadened or not. The exception to this is the broadened data set for Cr^{2+}, which show a larger dispersion in the fit parameters, particularly in the case of $10D_q$ and to a lesser extent also in the case of the hwhm parameter. In this regard, we found a correlation in the best fits between the parameters $10D_q$ and hwhm (see Figure S10), which indicates that for broadened spectra, it may be harder to define the crystal field parameters with low uncertainties. This is again observed for a couple of the data sets analyzed for Fe^{2+} (see below).

Fe Systems. In the case of the Fe^{2+} data sets, which are very sensitive to the spin-state in the ground state, as shown in Figure S3 and Figure 3, the algorithm is able to successfully find the right combination of parameters in all of the narrowed data sets. This means that $L_{2,3}$-edge XAS spectroscopy is very sensitive not only to the spin state but also to small variations in the crystal field, whenever there is a sufficient resolution of spectral features (Figures S11 and S12 show representative fits). Moreover, we also found that the developed adaptive grid algorithm is robust enough to find very localized solutions in most of the cases for the broadened data sets, with two exceptions: for the case of Fe^{2+} in D_{4h} symmetry with an intermediate-spin ($^3B_2$) ground state and for the case of the high-spin Fe^{2+} complex in octahedral symmetry. In both of these cases, we observed a significant deviation in the value of $10D_q$ from the actual values (see Tables S3 and S6). In addition, in the case of the Fe^{2+} in the intermediate-spin $^3B_2$,

https://doi.org/10.1021/acs.inorgchem.2c02830
Inorg. Chem. 2023, 62, 3738−3760

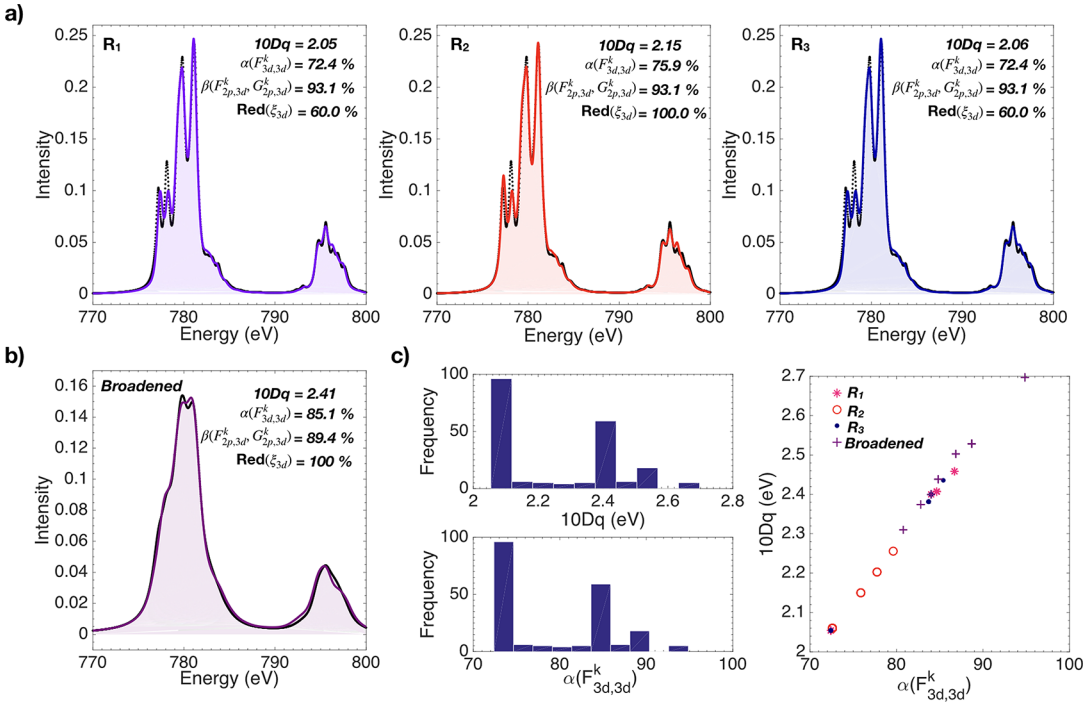

Figure 6. Representative fits for the fitting of crystal field simulations to the calculated data sets of Co^{2+} in an octahedral environment with $10D_q$ = 2.27 eV. (a) Representative fits for fit calculations R_1, R_2, and R_3 performed for the narrowed data set with hwhm = 0.3 eV. (b) Representative fit for the fitting of the broadened data set with hwhm = 0.8 eV. (c) Observed linear correlation between the fit values of $10D_q$ and $\alpha(F^k_{3d,3d})$ in all fit calculations.

we found an anticorrelation between the value of $10D_q$ and the value for hwhm (see Figure S13), which implies that by slightly broadening the spectrum more (in relation to its actual value), it is possible to recover some of the intensity that would be lost due to a smaller value of $10D_q$. In general we expect that, for broader spectra, similar correlations can be found. Moreover, in the case of the broadened data set of Cr^{2+}, for example, this would not imply that different solutions are actually found. Instead, one could say that the family of solutions around the mean for these parameters are a measure of the uncertainty of such parameters for spectra with poor resolution. This is not the case in the broadened data set of Fe^{2+} with the $^3B_2$ ground state, as it actually impacts the accuracy of the final result for $10D_q$ (see Table S6.) Furthermore, in the case of the broadened data set for the high-spin octahedral complex, we also observed localized solutions with a low dispersion for all crystal field parameters ($10D_q$ = 0.94 ± 0.01, D_s = 0.02 ± 0.01 eV, and D_t = −0.01 ± 0.01 eV), which represent a slightly different solution than the actual set of values originally employed to create this data set. To investigate this further, we calculated the $L_{2,3}$-edge XAS spectra for a series of Fe^{2+} complexes in octahedral symmetry with a value of $10D_q$ varying from 0.5 to 1.5 eV in steps of 0.1 eV. This series of simulations was calculated with two values of hwhm (0.3 and 0.8 eV). The results of these additional calculations are shown in Figures S18 and S19. In the vicinity of a $10D_q$ value of 1.0 eV (from about 0.8 to 1.1 eV), the spectra look in fact very similar, particularly in the case of the broadened data set. From this, it is clear that the adaptive grid algorithm is able to capture the differences in the spectra with different values of $10D_q$ only in the case of the narrowed data sets. To investigate this further, we use the crystal field parameters for the representative fit shown in Figure S11 (that is, $10D_q$ = 0.94 eV, D_s = 0.017 eV, and D_t = −0.012 eV) to run a single-point calculation in CTM4DOC. From this, we found that the ground state is composed of 100% the state $|e_g^{\ 3}b_{2g}^{\ 1}a_{1g}^{\ 1}b_{1g}^{\ 1}\rangle$ or ^5E with the first excited state (0.1 eV apart) being 100% $|b_{2g}^{\ 2}e_g^{\ 2}a_{1g}^{\ 1}b_{1g}^{\ 1}\rangle$ or $^5A_2$. At 10 K, this excited state is inaccessible (as weighted by the Boltzmann distribution). However, with $10D_q$ = 1.00, D_s = 0.00 eV, and D_t = 0.00 eV these two states would be equally probable at 10 K (weighted only by their multiplicities of 10 and 5, respectively). Thus, both will be contributing to the XAS spectrum. Therefore, the solution found by the adaptive grid algorithm in this case is fortuitous in the sense that other combinations of parameters (of $10D_q$, D_s, D_t, $\alpha(F^k_{3d,3d})$, $\beta(F^k_{2p,3d}, G^k_{2p,3d})$, and hwhm) will be able to *fine-tune* the spectral features within the vicinity of the region of $10D_q$ considered (between 0.8 and 1.1 eV).

From this, it can be envisaged that, for other similar cases where the spectra is relatively insensitive to small changes in electronic structure, in combination with a poor resolution of the spectral features, the adaptive grid algorithm will be able to find approximate solutions, or in other words, multiple solutions conveying a large uncertainty for the fit parameters. Importantly, all these possible solutions would be consistent with a common spin state, as the algorithm largely differentiate the obtained solutions for each of the spin states considered and given in Table S6.

On the other hand, as shown in Figure S14 and Table S7, the adaptive grid algorithm is also capable of finding the right composition in materials where more than one metallic site is present, even in the case where the spectra are rather broad with not as many resolved features (Figure S14b). In this regard, not only is the right proportion found in the case of the $4Fe^{3+}$:$3Fe^{2+}$ data sets but also the right combination of

https://doi.org/10.1021/acs.inorgchem.2c02830
Inorg. Chem. 2023, 62, 3738−3760

parameters for each component is found, even though the parameters found for Fe^{2+} exhibited a somewhat large dispersion. We investigated this further and found a moderate correlation between the parameter $\alpha(F^k_{3d,3d})$ and the value of $10D_q$ (see Figure S15), which imply that, at large values of $10D_q$ (relative to the corresponding Slater integrals), the spectra are relatively insensitive to changes in $10D_q$ near the solution in the sense that this is close to a strong-field scheme where the Slater integrals would have overall less influence.

Co^{2+} Mixed-Spin-State System. The case of the Co^{2+} data sets is yet another case where the original combination of parameters could not be found and where actually the solutions deviate the most from the original combination of parameters (see Tables S3 and S6). However, their collective analysis has revealed an interesting correlation which should not be unique to Co^{2+} but to any transition-metal complex in a near spin-crossover transition point.

As shown in Figure 6c, a clear linear correlation is drawn between the parameter $10D_q$ and $\alpha(F^k_{3d,3d})$ in all the fits that were calculated. To investigate this further, a total of three independent fitting calculations were performed in the case of the narrowed data set, labeled here as R_1, R_2, and R_3. In addition, the calculation for the broadened data set was fit only once. While the three calculations for the narrowed version converged nearly within the same region (particularly in the case of R_1 and R_3), the solution for the broadened spectra extrapolated the aforementioned correlation by finding solutions at proportionally higher values of $10D_q$ and $\alpha(F^k_{3d,3d})$. Then, a phase diagram calculation was performed using CTM4DOC[44] within the ranges of $10D_q$ and $\alpha(F^k_{3d,3d})$ obtained from these fits. This is shown in Figure 7, revealing that all of the solutions found lay within a region where a single spin state cannot be established. Clearly, the adaptive grid algorithm is helping reveal spin-crossover transition points in this case. Previously, Griffith,[47,48] Orgel[49] and König and Kremer[50] have established spin-pairing energies for d^3–d^7 transition-metal complexes, where a fixed ratio between the crystal field parameter $10D_q$ and the Racah parameter B is established for the spin-crossover transition point. Considering configuration interactions, König and Kremer found that the spin-pairing energy for a d^7 complex occurs when $10D_q/B$ = 19.42 for whenever the ratio between Racah parameters C and B is equal to $\gamma = C/B = 4.0$ and a value of $10D_q/B = 15.87$ for γ = 3.0.[50] Thus, using the relationship between Racah parameters, B and C, and the Slater integrals $F^2_{3d,3d}$ and $F^4_{3d,3d}$[1]

$$B = \frac{1}{49}F^2_{3d,3d} - \frac{5}{441}F^4_{3d,3d} \quad (34)$$

$$C = \frac{35}{441}F^4_{3d,3d} \quad (35)$$

and using the values listed in Table S3 for $F^2_{3d,3d}$ and $F^4_{3d,3d}$ used to calculate the spectra for Co^{2+}, we found a value of B = 0.124 eV and a value of C = 0.457 eV, which yields a γ ratio value of 3.69. Then, from eqs 34 and 35, it is evident that this ratio should remain the same in Co^{2+} as long as the scaling factors for $F^2_{3d,3d}$ and $F^4_{3d,3d}$ are set to be the same, such as in this case. Thus, a γ-weighted average for the spin-pairing energy is calculated for γ = 3.69, giving

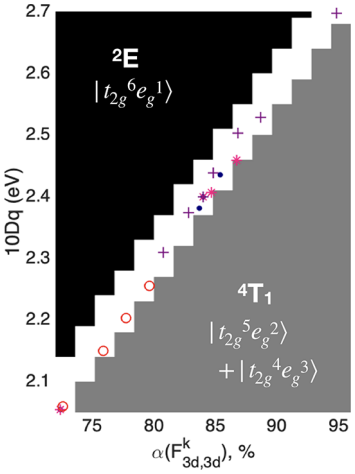

Figure 7. Phase diagram calculation for the ground-state of Co^{2+} in octahedral symmetry computed with a fixed value for the 3d spin–orbit coupling equivalent to 80% the Hartree–Fock value. The correlation discussed between $10D_q$ and $\alpha(F^k_{3d,3d})$ for Figure 6c) is also included. Areas shaded in gray correspond to a well-defined $^4T_1$ state ($E_{1/2}$, with ca. 96% $|t_{2g}{}^5e_g{}^2\rangle$ and 4% $|t_{2g}{}^4e_g{}^3\rangle$). Areas shaded in black correspond to a well-defined ^2E state ($G_{3/2}$, with ca. 100% $|t_{2g}{}^6e_g{}^1\rangle$). Areas shaded in white correspond to near spin-crossover transition points where the ground state is a combination of states.

Table 5. Composition of the First Two Multiplets in the Initial State for Octahedral Co^{2+} using the parameters obtained from the fit calculations to the narrowed data set (R_1, R_2, and R_3) and to the Broadened Data Set: (a) Compositions Calculated from the Set of Parameters of the Representative Fit of R_1 and/or R_3 Shown in Figure 6a; (b) Compositions Calculated from the Parameters of Representative Fit in R_2 (Figure 6a, middle); (c) Compositions Calculated from the Parameters of Representative Fit to the Broadened Data Set (Figure 6b)[a]

energy (eV)	multiplicity	O' term	cubic term	O_h crystal field configuration
(a) $R_1 \approx R_3$, $10D_q$ = 2.05 eV; $\alpha(F^k_{3d,3d})$ = 72.4 %; Red(ξ_{3d}) = 60%				
−3.617	2	$\Gamma_6(E_{1/2})$	$^4T_1$ 100%	$\|t_{2g}{}^5e_g{}^2\rangle$ 95.5%
				$\|t_{2g}{}^4e_g{}^3\rangle$ 4.5%
−3.615	4	$\Gamma_8(G_{3/2})$	$^4T_1$ 50.9%	$\|t_{2g}{}^5e_g{}^2\rangle$ 49.0%
			^2E 49.1%	$\|t_{2g}{}^6e_g{}^1\rangle$ 47.7%
				$\|t_{2g}{}^4e_g{}^3\rangle$ 3.3%
(b) R_2, $10D_q$ = 2.15 eV; $\alpha(F^k_{3d,3d})$ = 75.9%; Red(ξ_{3d}) = 100%				
−3.823	2	$\Gamma_6(E_{1/2})$	$^4T_1$ 100%	$\|t_{2g}{}^5e_g{}^2\rangle$ 95.5%
				$\|t_{2g}{}^4e_g{}^3\rangle$ 4.5%
−3.822	4	$\Gamma_8(G_{3/2})$	^2E 50.6%	$\|t_{2g}{}^6e_g{}^1\rangle$ 49.1%
			$^4T_1$ 49.4%	$\|t_{2g}{}^5e_g{}^2\rangle$ 47.4%
				$\|t_{2g}{}^4e_g{}^3\rangle$ 3.2%
(c) Broadened, $10D_q$ = 2.41 eV; $\alpha(F^k_{3d,3d})$ = 85.1%; Red(ξ_{3d}) = 100%				
−4.276	2	$\Gamma_6(E_{1/2})$	$^4T_1$ 100%	$\|t_{2g}{}^5e_g{}^2\rangle$ 95.5%
				$\|t_{2g}{}^4e_g{}^3\rangle$ 4.5%
−4.274	4	$\Gamma_8(G_{3/2})$	^2E 50.2%	$\|t_{2g}{}^6e_g{}^1\rangle$ 49.0%
			$^4T_1$ 49.8%	$\|t_{2g}{}^5e_g{}^2\rangle$ 47.3%
				$\|t_{2g}{}^4e_g{}^3\rangle$ 3.2%

[a]The two nearly degenerate low-lying multiplets in each case have the same collective composition as the ground state listed in Table 2b: that is, ca. 66% of $^4T_1$ and 33% of ^2E.

https://doi.org/10.1021/acs.inorgchem.2c02830
Inorg. Chem. 2023, 62, 3738−3760

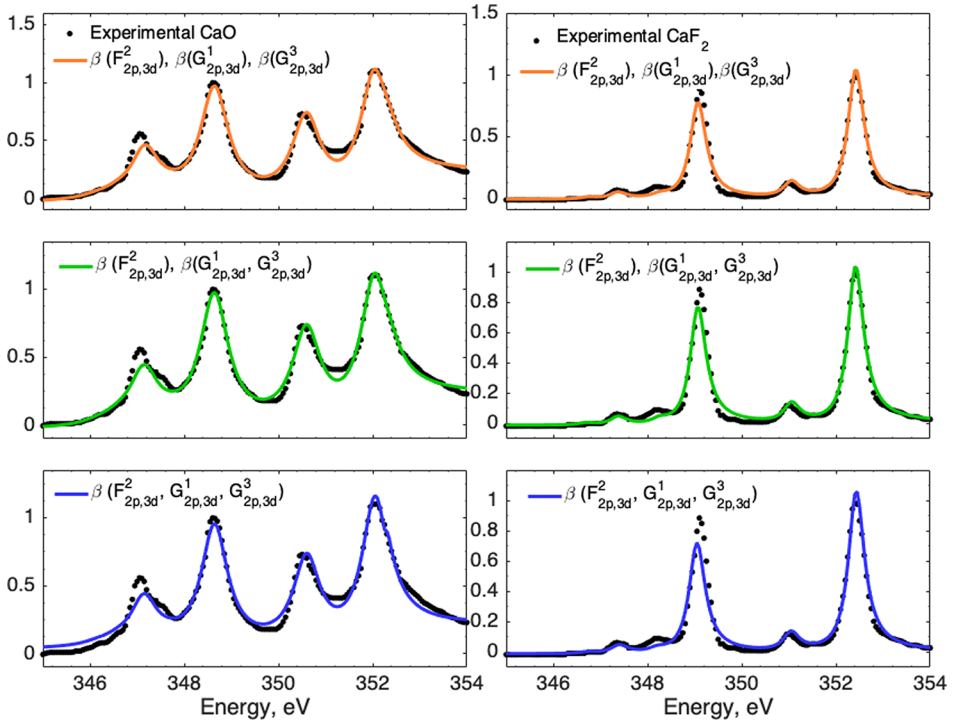

Figure 8. Average of fits of crystal-field multiplet simulations to the experimental Ca $L_{2,3}$-edge XAS data of CaO (left) and CaF_2 (right) for three different models: (1) with a single β parameter ($\beta(F^2_{2p,3d}, G^1_{2p,3d}, G^3_{2p,3d})$, top), (2) with two β parameters ($\beta(F^2_{2p,3d})$ and $\beta(G^1_{2p,3d}, G^3_{2p,3d})$, middle), and (3) with three β parameters ($\beta(F^2_{2p,3d})$, $\beta(G^1_{2p,3d})$ and $\beta(G^3_{2p,3d})$, bottom).

Table 6. Comparison of Results for Models 1−3 in the Fitting of Crystal Field Multiplet Simulations to Experimental Ca $L_{2,3}$-Edge XAS of CaO and CaF_2

parameter	model 1	model 2	model 3
		CaO	
$10D_q$	1.42 ± 0.01	1.44 ± 0.01	1.44 ± 0.01
$\beta(F^2_{2p,3d}, G^1_{2p,3d}, G^3_{2p,3d})$, %	71.3 ± 0.4		
$\beta(F^2_{2p,3d})$, %		69.8 ± 1.8	74.4 ± 2.1
$\beta(G^1_{2p,3d}, G^3_{2p,3d})$, %		67.2 ± 0.5	
$\beta(G^1_{2p,3d})$, %			68.7 ± 1.2
$\beta(G^3_{2p,3d})$, %			87.2 ± 5.0
		CaF_2	
$10D_q$	−0.81 ± 0.02	−0.81 ± 0.02	−0.80 ± 0.01
$\beta(F^2_{2p,3d}, G^1_{2p,3d}, G^3_{2p,3d})$, %	83.7 ± 1.4		
$\beta(F^2_{2p,3d})$, %		95.5 ± 0.4	92.3 ± 0.2
$\beta(G^1_{2p,3d}, G^3_{2p,3d})$, %		83.7 ± 1.0	
$\beta(G^1_{2p,3d})$, %			82.5 ± 0.5
$\beta(G^3_{2p,3d})$, %			65.6 ± 2.7

$$\frac{10D_q}{B} = 0.69(19.42) + 0.31(15.87) = 18.32 \quad (36)$$

This is a value in very good agreement with the ratio between $10D_q$ and B used to calculate the Co^{2+} data sets studied here. That is

$$\frac{10D_q}{B} = \frac{2.27}{0.124} = 18.21 \quad (37)$$

which is also the same ratio found in all fits lying in the nearly straight line shown in Figure 6. In other words, the slope for this straight line is directly related to the spin-pairing energy calculated by Kremer and König. Moreover, the composition of the ground state found for $10D_q = 2.27$ and $\alpha(F^k_{3d,3d}) = 80\%$ (see Table 2), in comparison to the composition found for the first two multiplets in the initial state of the fits shown in Figure 6 (see Table 5), reveals that indeed all these fits reflect a similar HS ($^4T_1$)−LS (^2E) composition of approximately 66% of $^4T_1$ and 33% of ^2E, leading to a very similar shape in the XAS spectrum, which is what ultimately *drives* the adaptive grid algorithm in finding the solutions discussed here. Finally, Figures S16 and S17 show that no other correlations are found during the fitting procedure with the other two grid parameters

https://doi.org/10.1021/acs.inorgchem.2c02830
Inorg. Chem. 2023, 62, 3738−3760

Table 7. Parameters Obtained in the Fitting of Crystal Field Multiplet Simulations to Experimental Ca $L_{2,3}$-Edge XAS of CaO and CaF_2 Using Model 2, Where Two Different Values of β Were Utilized: One to Reduce the the Hartree−Fock Value of the $F^2_{2p,3d}$ Integral and Another to Reduce the Hartree−Fock Value of the $G^1_{2p,3d}$,$G^3_{2p,3d}$ Integral[a]

crystal field		Slater integral		spin−orbit coupling		broadening	
			CaO				
$10D_q$	1.44 ± 0.01	$F^2_{2p,3d}$	2.65 ± 0.07 (69.8 ± 1.8%)	ξ_{2p}	2.40 (100%)	hwhm	0.36 ± 0.01
		$G^1_{2p,3d}$	1.69 ± 0.01 (67.2 ± 0.5%)	ξ_{3d}	0.011 (100%)	Gaussian weight	0%
		$G^3_{2p,3d}$	0.96 ± 0.01 (67.2 ± 0.5%)				
			CaF_2				
$10D_q$	−0.81 ± 0.02	$F^2_{2p,3d}$	3.63 ± 0.01 (95.5 ± 0.4%)	ξ_{2p}	2.40 (100%)	hwhm	0.20 ± 0.01
		$G^1_{2p,3d}$	2.10 ± 0.03 (83.7 ± 1.0%)	ξ_{3d}	0.011 (100%)	Gaussian Weight	17.6 ± 0.1%
		$G^3_{2p,3d}$	1.19 ± 0.01 (83.7 ± 1.0%)				

[a]The exact range of values for all the Slater integrals are listed. The spin−orbit coupling constants for Ca^{2+} were fixed to their Hartree−Fock calculated value.

that were fit (that is, $\beta(F^k_{2p,3d}, G^k_{2p,3d})$ and the reduction for ξ_{3d}). Importantly, the large uncertainty in $\beta(F^k_{2p,3d}, G^k_{2p,3d})$ further reveals that the refined solutions that were observed while fitting other data sets discussed above for all the fit parameters is largely obscured here by the sensitivity to the mixture of spin states. The same is true for the reduction in the 3d spin−orbit coupling. Even though the spin−orbit coupling operator is responsible for enabling the mixing of spin states in the first place, it is enough for it to be larger than zero for the mixing to occur at large near the spin-crossover transition point. That is why the distribution of the fits shown in Figure S17 reveals values for this reduction to be at least 20% (the next point after 0% in the initial grid), with solutions being found more frequently at higher values. This last observation is more likely related to temperature. It has been documented previously that each of the 4 states emerging from the $^4T_1$ multiplet due to spin−orbit coupling in the 3d shell (that is, $E_{1/2}$, $G_{3/2}$, $G_{3/2}'$, and $E_{5/2}$)[43,51] gives rise to a different $L_{2,3}$-edge XAS spectrum. Thus, the Boltzmann distribution of such states can dramatically change the shape of the spectrum depending on temperature. At 10 K, a reduction as low as 20% of the atomic 3d spin−orbit coupling seems to be enough to keep the first excited state sufficiently apart so that the dominant shape-defining mixing is indeed between the nearly degenerate $^4T_1$ and ^2E states comprising the ground state.

Ultimately, the fitting of the calculated data sets presented here broadly demonstrates the sensitivity of the adaptive grid algorithm to find unique solutions in most cases, except in those where the broadening may slightly impact the accuracy and precision in the outcome of the crystal field parameters, and more particularly in cases near a spin-crossover transition point for which the dominant driving factor is the mixing of spin states, where multiple combinations of crystal field and interelectronic repulsion parameters are found. These results also demonstrate that $L_{2,3}$-edge XAS is a very sensitive technique not only to the spin state but also to the fine details in the ground state, as implied by the very localized solutions for the crystal field parameters found in most of the cases presented here.

Experimental Data Sets. We have further tested the adaptive grid algorithm by fitting the experimental Ca $L_{2,3}$-edge XAS data of CaO, CaF_2 and of Mn $L_{2,3}$-edge XAS data of MnO, $LiMnO_2$ and Mn_2O_3.

CaO and CaF_2. CaO and CaF_2 are ionic materials with crystal lattice structures consisting of octahedral and tetrahedral sites, respectively. Thus, one of the parameters to fit is the crystal field parameter $10D_q$, which in the case of CaF_2 adopts a negative value. Moreover, in ionic compounds of Ca^{2+} there are no electron−electron interactions between 3d electrons and only the reduction of the 2p−3d interactions is required in the final state configuration ($2p^53d^1$). One can in addition distinguish the reduction in the interaction of 2p and 3d electrons. That is, use a single reduction parameter for the direct Coulomb interaction parameter $F^2_{2p,3d}$ and a different parameter to reduce the exchange parameters $G^1_{2p,3d}$, and $G^3_{2p,3d}$. Thus, we have explored three different models: (1) using a single β parameter ($9\beta(F^2_{2p_{9p,3d}}, G^1_{2p_{9p,3d}}, G^3_{2p,3d})$), (2) using two β parameters ($\beta(F^2_{2p,3d})$ and $\beta(G^1_{2p,3d}, G^3_{2p,3d})$), and (3) using three β parameters ($\beta(F^2_{2p,3d})$, $\beta(G^1_{2p,3d})$ and $\beta(G^3_{2p,3d})$). Figure 8 shows the results for the three case scenarios in both compounds, while Table 6 gives the obtained parameters for each of the three models in each compound. These results reveal an improvement when using two β parameters instead of one in the quality of the fits, especially in the case of CaO, for which the agreement between the fit simulations and the experimental data is significantly improved within the range of energy 346−350 eV. These results also show that the agreement of the simulations with the experimental data is insensitive to the use of three β parameters, in particular the reduction parameter $\beta(G^3_{2p,3d})$, based on its much larger uncertainty and the very similar result obtained when using only two β parameters. Overall, it is the second model which gives the best results in terms of the agreement between theory and experiment, which indicates that the use of a different reduction parameter for $F^2_{2p,3d}$ and collectively for $G^1_{2p,3d}$,$G^3_{2p,3d}$ could be of benefit for cases in which the number of fit parameters is not so large. In all cases, the reduction obtained

https://doi.org/10.1021/acs.inorgchem.2c02830
Inorg. Chem. 2023, 62, 3738−3760

Table 8. Parameters for the Fit Simulations of MnO, and $LiMnO_2$ to Their Experimental Mn $L_{2,3}$-Edge XAS Data[a]

crystal field		Slater integral		spin−orbit coupling		broadening	
				MnO			
$10D_q$	0.91 ± 0.01	$F^2_{3d,3d}$ (initial)	7.91 ± 0.02 (76.7 ± 0.2%)	ξ_{3d} (initial)	0.040 (100%)	hwhm (L_3)	0.31 ± 0.01
		$F^4_{3d,3d}$ (initial)	4.92 ± 0.01 (76.7 ± 0.2%)	ξ_{3d} (final)	0.053 (100%)	hwhm (L_2)	0.51 ± 0.01
		$F^2_{3d,3d}$ (final)	8.56 ± 0.02 (76.7 ± 0.2%)	ξ_{2p} (final)	6.845 (100%)	Gaussian weight	0%
		$F^4_{3d,3d}$ (final)	5.32 ± 0.01 (76.7 ± 0.2%)				
		$F^4_{2p,3d}$ (final)	5.17 ± 0.03 (81.8 ± 0.4%)				
		$G^1_{2p,3d}$ (final)	3.77 ± 0.02 (81.8 ± 0.4%)				
		$G^3_{2p,3d}$ (final)	2.14 ± 0.01 (81.8 ± 0.4%)				
				$LiMnO_2$			
$10D_q$	2.43 ± 0.07	$F^2_{3d,3d}$ (initial)	8.58 ± 0.29 (75.2 ± 2.5%)	ξ_{3d} (initial)	0.046 (100%)	hwhm (L_3)	0.35 ± 0.02
D_s	0.36 ± 0.02	$F^4_{3d,3d}$ (initial)	5.37 ± 0.18 (75.2 ± 2.5%)	ξ_{3d} (final)	0.059 (100%)	hwhm (L_2)	0.56 ± 0.03
D_t	0.13 ± 0.01	$F^2_{3d,3d}$ (final)	9.18 ± 0.31 (75.2 ± 2.5%)	ξ_{2p} (final)	6.845 (100%)	Gaussian Weight	0%
		$F^4_{3d,3d}$ (final)	5.75 ± 0.19 (75.2 ± 2.5%)				
		$F^2_{2p,3d}$ (final)	6.04 ± 0.11 (86.4 ± 1.6%)				
		$G^1_{2p,3d}$ (final)	4.47 ± 0.08 (86.4 ± 1.6%)				
		$G^3_{2p,3d}$ (final)	2.54 ± 0.05 (86.4 ± 1.6%)				

[a]Values for the Slater integrals are given in eV and as a percentage of the Hartree−Fock values. Spin−orbit coupling values were not scaled in these calculations.

is given with respect to their Hartree−Fock values. In terms of the size of the grid, all models contained a maximum of 1000 points, and took less than 1 day to complete 5 cycles. In all cases, a Lorentzian profile was used to optimize the broadening parameters, giving a fwhm for the second and third model of Γ = 0.724 ± 0.001 eV and of 0.662 ± 0.001 using the first model in the case of CaO. In the case of CaF_2 the transition lines are fit with a pseudo-Voigt profile with a fwhm of Γ = 0.404 ± 0.001 eV and η = 0.176 ± 0.001. The increased broadening observed for CaO in relation to CaF_2 is likely due to the need of charge-transfer effects in the case of CaO in order to increase the number of underlying transitions, without the need for a larger broadening. The overall better agreement of the fits to the experimental data of CaF_2 further confirms that for CaO an improved model with charge-transfer effects would be required to arrive at a better outcome. We emphasize here that for CaF_2 both of the reduction parameters are above the typical 80% used to reduce the Slater integrals in the free ions, which confirms the ionic nature of this compound. A full list of the obtained parameters from the second model in CaO and CaF_2 is provided in Table 7. Finally, in the case of CaO, for which the fit model needed an edge jump, such as that shown in Figure 1, the energy position of the first edge (E_I) was consistently settled at a higher energy during the fitting procedure of all three models, so that only one edge jump ended up being necessary in the considered energy range with E_I = 352.28 ± 0.03 eV for model 1, E_I = 352.27 ± 0.02 eV for model 2, and E_I = 352.25 ± 0.02 eV for model 3. On the other hand, in the case of CaF_2 no edge jump was necessary within the energy range studied, likely due to its highly ionic character, thus shifting the edge jumps to higher energy values.

MnO. In the case of MnO, three parameters are included in the grid: (1) α, the reduction of the $F^k_{3d,3d}$ Slater integrals, (2) β, the reduction of $F^2_{2p,3d}$, and $G^k_{2p,3d}$ parameters, and (3) the value of $10D_q$ (Table 8). We note here that a different reduction (with respect to Hartree−Fock values) is used for interactions involving only 3d electrons and those involving interactions between 2p and 3d electrons. This is because the interactions between valence electrons should get reduced more by covalency (nephelauxcetic effect). The grid used in this case was created with more than 2000 points, and the entire calculation (after 5 cycles of refinement) took less than 1 day, obtaining very localized solutions for each parameter, with very low uncertainties: $10D_q$ = 0.94 ± 0.01, $\alpha(F^k_{3d,3d})$ = 76.7 ± 0.2 %, and $\beta(F^k_{2p,3d}, G^k_{2p,3d})$ = 81.8 ± 0.4 % (see Figure 9, top). The reduction is about the same as the value estimated from experience (about 80%) to reach atomic values.

Moreover, the trustworthy reproduction of all spectral features, including those at the L_2-edge (the cluster of states at higher energies separated by the large 2p spin−orbit

https://doi.org/10.1021/acs.inorgchem.2c02830
Inorg. Chem. 2023, 62, 3738−3760

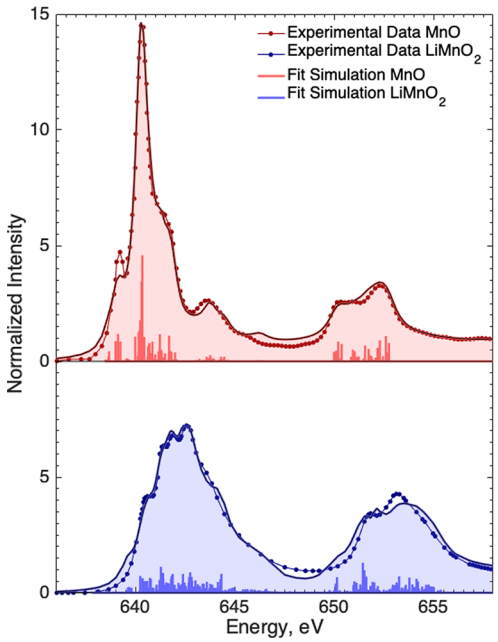

Figure 9. Average of best fits of crystal-field multiplet simulations to experimental Mn $L_{2,3}$-edge XAS data for complexes MnO (top), and $LiMnO_2$ (bottom).

coupling), is very remarkable using this simple model. Moreover, the inflection point (E_I) of the L_3-edge jump settled in good fits at E_I = 641.7 ± 0.01 eV. This is in principle unexpected, as this edge jump usually appears higher (with respect to the bound transitions) in other divalent metal oxides. Notably in the case of NiO, for example, XPS 1s data have been used in the past to establish the edge positions in its $L_{2,3}$-edge XAS data.[52] Considering this, even when this parameter is allowed to float initially (first cycle) only at higher energies (ca. 644 eV), during the fitting procedure these limits adjust back to lower energies during the adaptive grid algorithm. Figure S20 shows, for example, the fit edge position at E_I = 644.64 ± 0.01 obtained after 3 cycles for a calculation where the edge position is initially forced to adopt higher energy values. In addition, Figure S21 shows the corresponding representative fit simulation (including the edge jumps) to the experimental data after 3 cycles. However, when this calculation is finished (after 5 cycles), the fits again resemble the edge positions shown in Figure 1 and with the fit simulations again looking like that shown in Figure 9. Ultimately, this demonstrates that the energy position of the edge jump tries to compensate intensity not reflected by the crystal field multiplet simulation performed in this study. Despite the very close agreement, the overall agreement should be improved if charge transfer multiplet simulations are used in this case. This should, for example, improve the agreement for the fitting of the feature at ca. 639 eV. Ideally, another improvement is to include in the model the underlying background, particularly when the raw data are available. Otherwise, the propagation of errors during data reduction leads to modified data sets which can make the procedure of fitting edge jumps and simulations together more challenging.

$LiMnO_2$. In the case of $LiMnO_2$ (see Figure 9, bottom) the L_2-edge does not get reproduced on its entirety, but the reproduction of all features at the L_3-edge is also quite remarkable and to our knowledge the best reproduction of this spectrum. In this case, there were 5 simulation parameters (including the crystal field parameters D_s and D_t) and hence the use of a grid of nearly 2000 points was necessary. The total calculation time is less than 2 days, and again, the obtained results indicate well-localized parameters as oppose to several families of possible solutions, giving $10D_q$ = 2.43 ± 0.07, D_s = 0.36 ± 0.02 eV, and D_t = 0.13 ± 0.01 eV, with $\alpha(F^k_{3d,3d})$ = 81 ± 2 %, and $\beta(F^k_{2p,3d}, G^k_{2p,3d})$ = 86 ± 2 %. Moreover, in these fits, the inflection point of the edge jump was found at E_I = 651.90 ± 0.07 eV. We emphasize here that the results in this particular case show how the method is able to detect distortion parameters with small uncertainties, in a way similar to that in the analysis of the narrowed version of the calculated data sets discussed above. The methodology presented in this work shows that the interpretation of experimental $L_{2,3}$-edge XAS data for simple ionic materials such as CaO, MnO, and CaF_2 can be expedited, making it possible to also evaluate uncertainties for the radial parameters and to assess if multiple solutions could really exist based on the exploration of a large solution space. In addition, this example also shows that the adaptive grid algorithm is robust and sensitive to evaluate distortion parameters D_s and D_t in experimental data, which otherwise can be a daunting and very time-consuming task. Precisely because of this difficulty, an early analysis of the data for $LiMnO_2$ suggested the mixing of spin states ($^5B_2$ and ^3E) in the ground state in order to explain the observed shape of the spectrum[43] without explaining the very significant Jahn−Teller distortion, something that became evident later for this material. The results obtained here for $LiMnO_2$ are indeed consistent with a large Jahn−Teller distortion, as shown in the crystal-field diagram of Figure 10 deduced from the obtained crystal field parameters, $10D_q$, D_s, and D_t. A rough measure of the distortion is the very large separation of b_{1g} and a_{1g}, which in the case of a perfect octahedral complex would be zero. A follow-up analysis of the

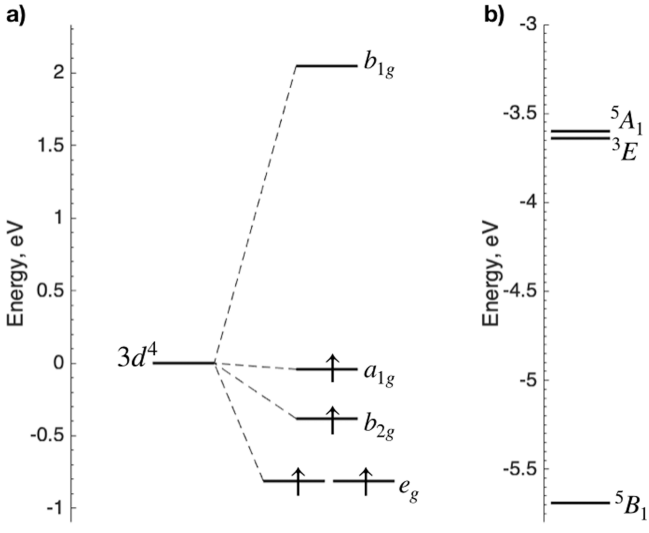

Figure 10. (a) Crystal-field diagram for $LiMnO_2$ showing a tetragonal distortion on going from a purely octahedral O_h complex to a D_{4h} complex with parameters $10D_q$ = 2.43, D_s = 0.36, and D_t = 0.13. The ground state is a well-defined $^5B_1$ composed of 100% of the crystal-field configuration $|e_g^2 b_{2g}^1 a_{1g}^1 b_{1g}^0\rangle$, as obtained from CTM4DOC. (b) The ground state depicted in (a) is substantially separated in energy, at ca. 2.1 eV, from other low-lying multiplets, ^3E and $^5A_1$, consistent with a well-defined ground state.

https://doi.org/10.1021/acs.inorgchem.2c02830
Inorg. Chem. 2023, 62, 3738−3760

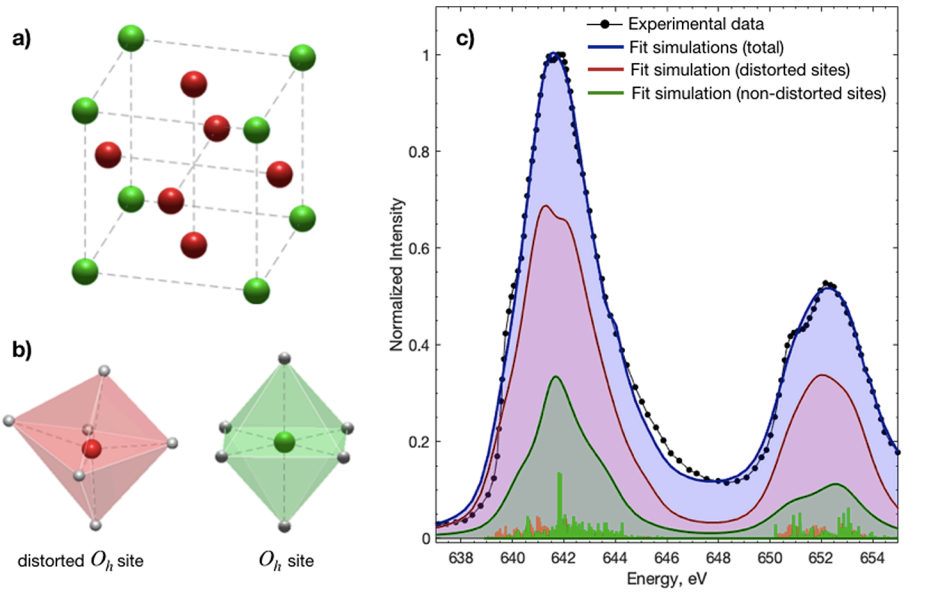

Figure 11. (a) Approximate location of the distorted and nondistorted Mn^{3+} sites within a FCC unit cell of Mn_2O_3. (b) Structural detail of distorted versus nondistorted Mn^{3+} in Mn_2O_3. (c) Average of best fits of crystal-field multiplet simulations to the experimental Mn $L_{2,3}$-edge XAS data of Mn_2O_3.

Table 9. Parameters for the Average of Good Fits of Crystal Field Multiplet Simulations to the Experimental Mn $L_{2,3}$-Edge XAS Spectrum of Mn_2O_3[a]

crystal field		Slater integral		spin−orbit coupling		broadening	
$10D_q$	1.28 ± 0.01	$F^2_{3d,3d}$ (initial)	4.54 ± 0.15 (39.8 ± 1.3%)	ξ_{3d} (initial)	0.040 (100%)	hwhm (L_3)	0.66 ± 0.08
z	1.67 ± 0.15	$F^4_{3d,3d}$ (initial)	2.85 ± 0.09 (39.8 ± 1.3%)	ξ_{3d} (final)	0.059 (100%)	hwhm (L_2)	0.90 ± 0.06
ζ_{3d}	6.25 ± 0.22	$F^2_{3d,3d}$ (final)	4.86 ± 0.15 (39.8 ± 1.3%)	ξ_{2p} (final)	6.845 (100%)	Gaussian Weight	36.8 ± 10.9%
		$F^4_{3d,3d}$ (final)	3.05 ± 0.10 (39.8 ± 1.3%)				
composition							
SF_1[b] (distorted)	1.74 ± 0.04	$F^2_{2p,3d}$ (final)	4.66 ± 0.2 (66.6 ± 2.9%)				
SF_2[b] (nondistorted)	0.57 ± 0.05	$G^1_{2p,3d}$ (final)	3.45 ± 0.15 (66.6 ± 2.9%)				
ratio	3.1 ± 0.4	$G^3_{2p,3d}$ (final)	1.96 ± 0.09 (66.6 ± 2.9%)				

[a]For the crystal field parameters, the $10D_q$ value corresponds to the contribution of the nondistorted site while the values of z and ζ_{3d} correspond to the contribution of the distorted site. [b]SF_1 and SF_2 account for the scaling factors of the crystal field simulations corresponding to the distorted and nondistorted sites, respectively.

multiplet structure using CTM4DOC[44] with these crystal-field parameters in combination with the average values obtained for reduction parameters in the Slater integrals ($\alpha(F^k_{3d,3d}$, and $\beta(F^k_{2p,3d}, G^k_{2p,3d})$) reveals a ground state corresponding to $^5B_1$ and composed of 100% the crystal-field configuration $|e_g^2 b_{2g}^1 a_{1g}^1 b_{1g}^0\rangle$. This is in fact a very well-defined ground state where the 5 states comprising this multiplet are ca. 2.1 eV apart from the closest two multiplets: ^3E (composed of 92% of $|e_g^3 b_{2g}^1 a_{1g}^0 b_{1g}^0\rangle$, 4% of $|e_g^1 b_{2g}^1 a_{1g}^2 b_{1g}^0\rangle$ and 2% of $|e_g^3 b_{2g}^0 a_{1g}^1 b_{1g}^0\rangle$) and $^5A_1$ (composed of 100% of the crystal-field state $|e_g^2 b_{2g}^1 a_{1g}^0 b_{1g}^1\rangle$). The difference in energy between the ground-state $^5B_1$ multiplet and the $^5A_1$ multiplet of 2.09 eV, which effectively corresponds to the transition of the unpaired electron in the d_{z^2} orbital to the $d_{x^2-y^2}$ orbital, is equivalent in energy to $4D_s + 5D_t = 4(0.36) + 5(0.13)$. This result is in good agreement with previous results from diffuse reflectance data collected on $LiMnO_2$, which is consistent with an energy gap of 1.92 eV.[53] Ultimately, this analysis reveals a very large distortion in $LiMnO_2$ which explains the damage that may be occurring in recharging batteries based on this material upon changing the oxidation state of Mn back and forth between Mn^{4+} and Mn^{3+}. Recent studies have in fact proposed different architectures to counterbalance the effect of this large distortion in the deformation of these batteries.[39,40]

Mn_2O_3. Mn_2O_3 adopts the structure of the mineral bixbyite and contains two different Mn^{3+} sites in its crystal structure.

https://doi.org/10.1021/acs.inorgchem.2c02830
Inorg. Chem. 2023, 62, 3738−3760

Both of the sites are in an octahedral environment, but one of them is highly distorted, while the other is in a nearly perfect O_h symmetry.[54−56] Figure 11a shows the location of the Mn sites within an approximate FCC unit cell (excluding the location of the oxygen atoms for clarity), while Figure 11b shows structural details around each site, contrasting the structure of the distorted site with the site in a nearly O_h symmetry (which we further refer to here as the nondistorted site). According to Figure 11a, the proportion of distorted to nondistorted sites in the structure of Mn_2O_3 should be close to a 3:1 ratio. From the fit results, the estimated proportion between both of these sites is deduced from the scaling factors of the corresponding fit simulations. Remarkably, from the obtained fits (Figure 11c), we have found a proportion of 3.1 ± 0.4 (Table 9), in close agreement with the expected value. Furthermore, according to previous studies, the magnetic properties of Mn_2O_3 are dependent on temperature, with the magnetic moment becoming zero above 80 K, while the magnetic ordering is consistent with a collinear model deduced from neutron diffraction data at low temperatures. This model couples the spins of Mn^{3+} collectively for the nondistorted sites, and in three separate groups it couples the spins for the distorted sites.[57] This means that the spin states for the distorted and nondistorted sites in this material do not have to be the same, which implies that, because of this derived arrangement, the different Mn^{3+} sites can have different spin states and still produce no magnetic field above 80 K. Thus, this example further illustrates that the methodology described in this work is useful to determine composition as well, for example in doped or composite materials or in mixtures of compounds where the existence of several type of sites is expected.

To properly simulate the contribution of the highly distorted Mn^{3+} site to the Mn $L_{2,3}$-edge XAS spectrum of Mn_2O_3, the crystal field potential is modeled using eq 2 by taking as a reference the geometry of one of the highly distorted sites from previous studies,[56] as an approximation to the representation of all the nondistorted sites in the material. The corresponding crystal field potential for this site is given then by eq 38, where the coefficients $A_{km}^{\ j}$ for each of the six oxygen atoms surrounding the Mn site are given in Table S9 and evaluated from the x, y, and z coordinates of the oxygen ligands in the structure provided in Table S10.

$$\begin{aligned}\hat{V}^{\mathrm{CF}} = &\sum_j^6 ze^2\frac{r^2}{a_j^3}(A^j_{2,-2}C_2^{-2} + A^j_{2,-1}C_2^{-1} + A^j_{2,0}C_2^0 \\ &+ A^j_{2,1}C_2^1 + A^j_{2,2}C_2^2) \\ &+ \sum_j^6 ze^2\frac{r^4}{a_j^5}(A^j_{4,-4}C_4^{-4} + A^j_{4,-3}C_4^{-3} + A^j_{4,-2}C_4^{-2} \\ &+ A^j_{4,-1}C_4^{-1} + A^j_{4,2}C_4^2 + A^j_{4,3}C_4^3 + A^j_{4,4}C_4^4)\end{aligned} \quad (38)$$

Moreover, the radial part of the potential was used together with a hydrogen-like single-ζ radial function scaled by ζ_{3d} according to eq 20, in order to evaluate the matrix elements corresponding to the crystal field potential. Thus, for the distorted site, instead of optimizing the crystal field parameters (e.g., $10D_q$, D_s, D_t), the fitting of the corresponding simulation requires the optimization of z and ζ_{3d} as grid parameters. The parameter z represents the absolute average value of the charge of the oxygen ligands surrounding the distorted Mn^{3+} sites, for which we initially used a range of 1.0−1.8 in steps of 0.2 (see Table 4). Furthermore, in the case of the parameter ζ_{3d}, we initially used a range of 5.5−6.5 in steps of 0.2. We based this initial range on the ζ_{3d} value calculated from Slater rules for 3d electrons in Mn^{3+}, which corresponds to a value of 5.95 for the initial state configuration. We note here that a_i, which is the distance between Mn and each of the oxygen atoms, is not a parameter to optimize but instead a value calculated directly from the crystal structure given in Table S10. Meanwhile, for the nondistorted site, we used the standard crystal-field potential for which we fit its $10D_q$ value. Common reduction factors for $\alpha(F^k_{3d,3d})$ and $\beta(F^k_{2p,3d}, G^k_{2p,3d})$ were used for both sites. Table 4 gives all the ranges and step sizes for all parameters included in the grid and optimized using the adaptive grid algorithm. Figure 11c shows the average of fit crystal multiplet simulations for the distorted and nondistorted O_h Mn^{3+} sites to the experimental Mn $L_{2,3}$-edge XAS, and Table 9 gives the results for all fit parameters using this model. Moreover, the inflection point of the first edge jump within the good fits (which averages the contributions from both Mn^{3+} sites) was found at 645.04 ± 1.99 eV, thus not a very well-defined edge-jump position in this case.

Even though the reproduction of the experimental data is reasonable, we note that the absence of many features in the experimental data would tend to increase the uncertainty of the parameters and the chances of getting multiple solutions by using different models. In cases like this, where spectral features are not well resolved, fitting at least another set of data when available (for example, X-ray magnetic circular dichroism (XMCD) or X-ray magnetic linear dichroism (XMLD)) together with the XAS would reduce the levels of uncertainty and would allow a discrimination between several possible models. In this case, the proportion found for the fit scaling factors of both simulations nearly reproducing the 3:1 proportion from the crystal structure is a good marker for this result but should not be taken as definitive. In this regard, not all fits that were found have the same 3:1 ratio (which is evident from the significant standard deviation of 0.4), which implies that some of them deviate considerably despite having a low SSE value. Figure 12a shows a phase diagram for octahedral Mn^{3+} in the vicinity of the solutions found for $10D_q$ and the reduction parameter, $\alpha(F^k_{3d,3d})$, showing also the distribution of fits within the span of these parameters. We found that all the solutions lay within a spin-crossover region similar to the case of octahedral Co^{2+}, but a bit more complicated, as there are more states interacting. We have then classified the fits according to the composition of their ground state, in terms of the mixing of cubic term symbols ^5E and $^3T_1$ and/or octahedral crystal field configurations, $|t_{2g}^{\ 3}e_g^{\ 1}\rangle$ and $|t_{2g}^{\ 4}e_g^{\ 0}\rangle$. A representative fit for each family of fits is labeled as (1)−(4). From these, the fit with a higher contribution of ^5E in the ground state is (1) with 84% of ^5E and only 16% of $^3T_1$. To explore in more detail the mixing of spin states in the low-lying multiplets found around this region, we also calculated Tanabe−Sugano diagrams with $\alpha(F^k_{3d,3d})$ = 38.2% (Figure 12b, top) and $\alpha(F^k_{3d,3d})$ = 39.5% (Figure 12b, bottom), both with respect to Hartree−Fock values. These diagrams show the splitting of 5 states emerging from the ^5E multiplet due to the 3d spin−orbit coupling. In the O' double group, the spin angular momentum basis for S = 2 in the ^5E multiplet transforms as the irreducible representations $\Gamma_3(E)$ and $\Gamma_5(T_2)$

https://doi.org/10.1021/acs.inorgchem.2c02830
Inorg. Chem. 2023, 62, 3738−3760

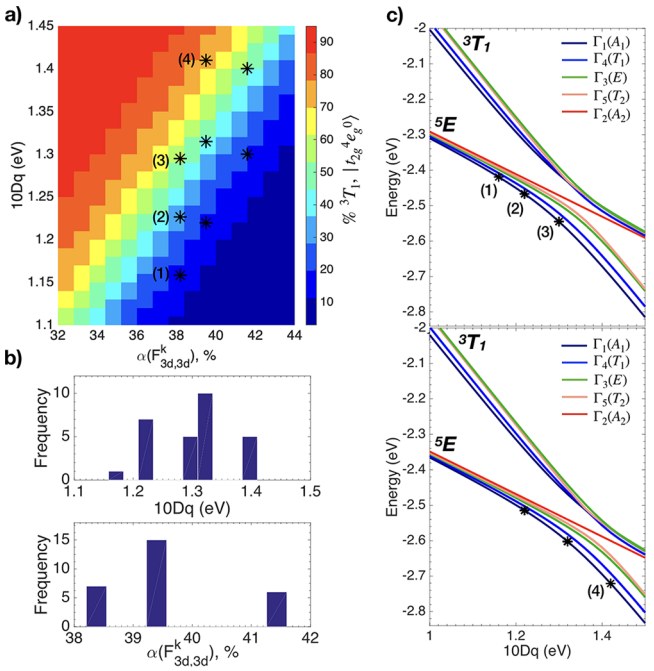

Figure 12. (a) Phase diagram for the undistorted O_h Mn^{3+} site in Mn_2O_3 in the vicinity of the solutions found for $10D_q$ and $\alpha(F^k_{3d,3d})$, showing their dispersion within the best fits. Fits labeled (1)−(4) are representative solutions with unique $10D_q/\alpha(F^k_{3d,3d})$ ratios and mixing compositions. (b) Distribution of fits according to their values of $10D_q$ and $\alpha(F^k_{3d,3d})$. (c) Tanabe−Sugano diagrams for the low-lying multiplets in O_h Mn^{3+} for varying $10D_q$ values ranging from 1.1 to 1.45 eV calculated at a value of $\alpha(F^k_{3d,3d})$ = 38.2% (top) and at a value of 39.5% (bottom) with respect to Hartree−Fock values.

(see Table S1). Thus, from the direct product with the E term corresponding to the orbital angular momentum part, 5 states with the following symmetries are obtained:

$$\begin{bmatrix}\Gamma_3\\ \Gamma_5\end{bmatrix} \otimes \Gamma_3 = \begin{bmatrix}\Gamma_1 \oplus \Gamma_2 \oplus \Gamma_3\\ \Gamma_4 \oplus \Gamma_5\end{bmatrix} \quad (39)$$

In a similar way, the spin angular momentum basis for $S = 1$ in the $^3T_1$ term transforms as the irreducible representation $\Gamma_4(T_1)$. Then, from the direct product with the T_1 term corresponding to the orbital angular momentum part, 4 states are derived (see Table S2):

$$\Gamma_4 \otimes \Gamma_4 = \Gamma_1 \oplus \Gamma_3 \oplus \Gamma_4 \oplus \Gamma_5 \quad (40)$$

This means that the states Γ_1, Γ_3, Γ_4, and Γ_5 are allowed to mix through the 3d spin−orbit coupling operator, while the Γ_2 state remains pure. Table 10 shows the extent to which each of these multiplets are mixed in the ground state for fits (1)−(4). Moreover, the undistorted O_h Mn^{3+} contribution in the $L_{2,3}$ XAS spectrum of Mn_2O_3 is a combination of the XAS originating from the first five states weighted by the Boltzmann distribution. The fits (1)−(4) along with the distorted and nondistorted site contributions are shown in Figures S22a−S25a, while the contributions to the undistorted spectrum from the first five low-lying states (Γ_1, Γ_4, Γ_3, Γ_5, and Γ_2) in fits (1)−(4) are provided in Figures S22b,c−S25b,c. Moreover, the Boltzmann factors used to scale the spectra originated from these states are provided in Table 10.

Ultimately, the final shape in the contribution of the nondistorted O_h Mn^{3+} site is very similar in fits (1)−(4) but different enough to arrive to different proportions in the scaling factors between the XAS of distorted and the nondistorted sites. From this, fit (1) is the closest to a ratio of 3 with a value of 2.98, compared to 2.78 in case of fit (2), 2.88 in the case of fit (3), and 3.66 in the case of fit (4). Taking

Table 10. Composition of the First Five Multiplets in the O_h Mn^{3+} Site According to the Parameters in Fits (1)−(4)

energy (eV)	multiplicity	O' term	cubic term	Boltzmann factor
(a) Fit (1): $10D_q$ = 1.16 eV; $\alpha(F^k_{3d,3d})$ = 38.2 %				
−2.418	1	$\Gamma_1(A_1)$	^5E ($t_{2g}^3e_g^1$), 84%	1.00
			$^3T_1$ ($t_{2g}^4e_g^0$), 16%	
−2.407	3	$\Gamma_4(T_1)$	^5E ($t_{2g}^3e_g^1$), 90%	0.65
			$^3T_1$ ($t_{2g}^4e_g^0$), 10%	
−2.397	2	$\Gamma_3(E)$	^5E ($t_{2g}^3e_g^1$), 95%	0.44
			$^3T_1$ ($t_{2g}^4e_g^0$), 5%	
−2.392	3	$\Gamma_5(T_2)$	^5E ($t_{2g}^3e_g^1$), 97%	0.36
			$^3T_1$ ($t_{2g}^4e_g^0$), 3%	
−2.386	1	$\Gamma_2(A_2)$	^5E ($t_{2g}^3e_g^1$), 100%	0.29
(b) Fit (2): $10D_q$ = 1.23 eV; $\alpha(F^k_{3d,3d})$ = 38.2%				
−2.472	1	$\Gamma_1(A_1)$	^5E ($t_{2g}^3e_g^1$), 71%	1.00
			$^3T_1$ ($t_{2g}^4e_g^0$), 29%	
−2.456	3	$\Gamma_4(T_1)$	^5E ($t_{2g}^3e_g^1$), 81%	0.54
			$^3T_1$ ($t_{2g}^4e_g^0$), 19%	
−2.442	2	$\Gamma_3(E)$	^5E ($t_{2g}^3e_g^1$), 91%	0.31
			$^3T_1$ ($t_{2g}^4e_g^0$), 9%	
−2.435	3	$\Gamma_5(T_2)$	^5E ($t_{2g}^3e_g^1$), 95%	0.24
			$^3T_1$ ($t_{2g}^4e_g^0$), 5%	
−2.427	1	$\Gamma_2(A_2)$	^5E ($t_{2g}^3e_g^1$), 100%	0.17
(c) Fit (3): $10D_q$ = 1.30 eV; $\alpha(F^k_{3d,3d})$=38.2 %				
−2.540	1	$\Gamma_1(A_1)$	^5E ($t_{2g}^3e_g^1$), 51%	1.00
			$^3T_1$ ($t_{2g}^4e_g^0$), 49%	
−2.517	3	$\Gamma_4(T_1)$	^5E ($t_{2g}^3e_g^1$), 60%	0.41
			$^3T_1$ ($t_{2g}^4e_g^0$), 40%	
−2.493	2	$\Gamma_3(E)$	^5E ($t_{2g}^3e_g^1$), 78%	0.16
			$^3T_1$ ($t_{2g}^4e_g^0$), 22%	
−2.482	3	$\Gamma_5(T_2)$	^5E ($t_{2g}^3e_g^1$), 84%	0.10
			$^3T_1$ ($t_{2g}^4e_g^0$), 16%	
−2.468	1	$\Gamma_2(A_2)$	^5E ($t_{2g}^3e_g^1$), 100%	0.06
(d) Fit (4): $10D_q$ = 1.40 eV; $\alpha(F^k_{3d,3d})$ = 39.5%				
−2.708	1	$\Gamma_1(A_1)$	$^3T_1$ ($t_{2g}^4e_g^0$), 72%	1.00
			^5E ($t_{2g}^3e_g^1$), 28%	
−2.680	3	$\Gamma_4(T_1)$	$^3T_1$ ($t_{2g}^4e_g^0$), 67%	0.33
			^5E ($t_{2g}^3e_g^1$), 33%	
−2.643	2	$\Gamma_3(E)$	$^3T_1$ ($t_{2g}^4e_g^9$), 51%	0.08
			^5E ($t_{2g}^4e_g^0$), 49%	
−2.630	3	$\Gamma_5(T_2)$	$^3T_1$ ($t_{2g}^4e_g^0$), 54%	0.05
			^5E ($t_{2g}^3e_g^1$), 46%	
−2.594	1	$\Gamma_2(A_2)$	^5E ($t_{2g}^3e_g^1$), 100%	0.01

https://doi.org/10.1021/acs.inorgchem.2c02830
Inorg. Chem. 2023, 62, 3738−3760

this additional criterion, we can assume that only the solutions equivalent to fit (1) are correct. This criterion extends to the additional fits lying along the same diagonal as fit (1) (in Figure 12a that would be all fits with a constant $10D_q/\alpha(F^k_{3d,3d})$ ratio), This does not necessarily imply that that all the solutions with the same $10D_q/\alpha(F^k_{3d,3d})$ ratio and equivalent in composition to fit (1) are the only viable solutions here, but it is a helpful piece of information used here to identify the most likely solutions.

On the other hand, the very strong reduction found here for $\alpha(F^k_{3d,3d})$ is likely imposed by the dominant contribution to the XAS, which is coming from the distorted sites. Thus, a follow-up analysis of the ground state in the distorted site using the average values of Table 9, is consistent with the crystal field diagrams of Figure 13a and the multiplet structure of the first few states of Figure 13b. In the case of the distorted site, the labels used in Figure 13b correspond to the dominant cubic term symbol $^5T_2$, which is practically pure for the ground state. This is a rather unusual ground state for an octahedral complex and is typical of high-spin T_d complexes. The inspection of a standard Tanabe−Sugano diagram for d^4 identifies the ground state as either the cubic term symbol ^5E in high-spin complexes or the cubic term symbol $^3T_1$ in low-spin complexes, which are the two states mixed in the undistorted site. In this case, the ground state is a well-defined state consistent with the crystal-field diagram of Figure 13a, where each of the $3d_i$ orbitals are now a linear combinations of the well-known octahedral set ($3d_{xy}$, $3d_{xz}$, $3d_{yz}$, $3d_{z^2}$, $3d_{x^2-y^2}$) or alternatively a linear combination of the complex spherical harmonics Y_2^{-2}, Y_2^{-1}, Y_2^0, Y_2^1, and Y_2^2, in combination with a radial function, R_{3d}. Using the crystal-field potential given in eq 38 with coefficients A_{km}^j of Table S9 and the average values obtained for z and ζ_{3d} from Table 9, the linear combinations given in Table 11 are obtained for each of the five 3d orbitals in the distorted site.

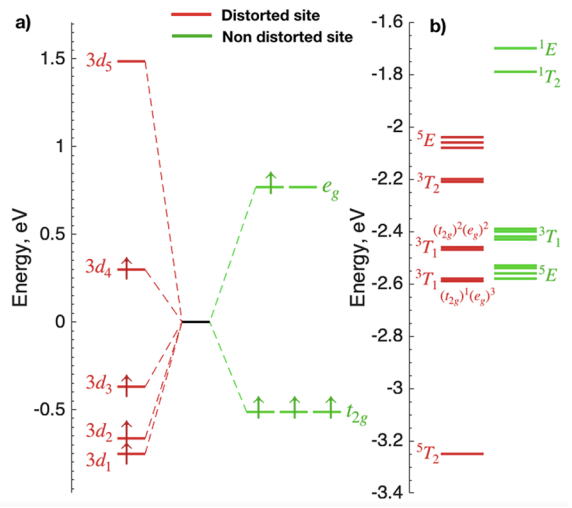

Figure 13. (a) Crystal field diagrams for the distorted and nondistorted sites of Mn^{3+} in Mn_2O_3 as obtained from the analysis of the ground state of each site. (b) Energy diagram showing the multiplet structure of the first few states, as obtained from the fit parameters of Table 9. The ground-state analysis of the highly distorted Mn^{3+} site is consistent with 100% of the cubic term symbol $^5T_2$ and the crystal field configuration $(t_{2g})^2(e_g)^2$. The ground-state analysis of the undistorted Mn^{3+} site is consistent with a mixture of a high-spin state ^5E, $(t_{2g})^3(e_g)^1$, and a low-spin state $^3T_1$, $(t_{2g})^4(e_g)^0$.

Table 11. 3d Orbitals for the Highly Distorted Site of Mn^{3+} in Mn_2O_3 Expressed as a Linear Combination of Spherical Harmonics Y_2^{-2}, Y_2^{-1}, Y_2^0, Y_2^1, and Y_2^2 in Combination with a 3d Radial Function, as Obtained from the Ground-State Analysis According to the Fit Results Given in Table 9 for the Distorted Mn^{3+} Site[a].

$$\psi_{3d} = R_{3d}\left(c_1Y_2^{-2} + c_2Y_2^{-1} + c_3Y_2^0 + c_4Y_2^1 + c_5Y_2^2\right)$$

	Orbital	Energy, eV	$\lvert c_1\rvert^2$, %	$\lvert c_2\rvert^2$, %	$\lvert c_3\rvert^2$, %	$\lvert c_4\rvert^2$, %	$\lvert c_5\rvert^2$, %
	ψ_{3d_1}	-0.75	1.9	47.8	0.5	47.8	1.9
	ψ_{3d_2}	-0.66	34.5	2.0	27.1	2.0	34.5
	ψ_{3d_3}	-0.37	20.6	0.2	58.4	0.2	20.6
	ψ_{3d_4}	0.30	43.0	0.1	13.9	0.1	43.0
	ψ_{3d_5}	1.49	0.0	50.0	0.0	50.0	0.0

[a]The locations of the point charges are shown as reference from the structure given in Table S10.

From this, while the first 4 orbitals imply linear combinations of the octahedral orbitals, the fifth orbital appears to be relatively pure and corresponds to the orbital $3d_{xz}$ using the framework of the structure provided in Table S10. As this orbital coincides directly with the location of 4 of the 6 point charges, this is then the most unstable 3d of the set and unlikely to be occupied. All of this translates into the unusual stabilization of the octahedral crystal field configuration $(t_{2g})^2(e_g)^2$, which explains the unusual shape for the contribution of the distorted site into the Mn $L_{2,3}$-edge XAS spectrum. The electronic structure described above for both of the Mn sites considers a common $\alpha(F^k_{3d,3d})$ parameter, which appears to be very low compared to other metal oxides, including $LiMnO_2$. Thus, as stated above, other solutions with higher values of $10D_q$ and $\alpha(F^k_{3d,3d})$ for the nondistorted site cannot be discarded, as these solutions can be obtained, for example, by using an independent $\alpha(F^k_{3d,3d})$ parameter for each site. Moreover, a refined radial 3d function with an increased level of theory (other than using the single-ζ used here) can also be employed. Another modification for the model is the possibility of quenching the 3d spin−orbit 3d coupling as another way to modulate the Boltzmann factors that weight the contributions for the nondistorted sites. Ultimately, what this example illustrates is that whenever the $L_{2,3}$-edge XAS spectrum is relatively featureless and there are many options in the model for both of the metallic sites, the multiple solution situation is difficult to rule out and the actual electronic structure is difficult to assess. Moreover, the analysis of these types of spectra will always need a careful follow-up analysis of these solutions, as illustrated here, and of additional evidence (data sets) to rule out some of the solutions.

https://doi.org/10.1021/acs.inorgchem.2c02830
Inorg. Chem. 2023, 62, 3738−3760

CONCLUSION AND FUTURE DEVELOPMENTS

In this work, we propose a new methodology to analyze $L_{2,3}$-edge XAS spectra of transition-metal complexes. This involves first the fitting of crystal-field multiplet simulations to the experimental data using an adaptive grid algorithm. Then, it also involves a follow-up analysis of the ground state based on the fit parameters to deduce the electronic structure of the studied complexes. We first fit calculated data sets for d^0-d^7 systems for which the parameters are known in advance in order to test how effective the adaptive grid algorithm is in finding the solutions. We further tested how robust the algorithm is when the same set of calculations are purposely broadened with a hwhm parameter of 0.8 eV. These examples highlighted the sensitivity of $L_{2,3}$-edge XAS spectroscopy, not only to the spin state but also to the fine details in electronic structure that come from slightly different crystal fields, and they further demonstrate that the adaptive grid algorithm is effective in finding unique spin-state solutions in practically all cases, except for the Co^{2+} system, for which a mixture of states was induced through 3d spin−orbit coupling. In such a case, the adaptive grid algorithm found a very strong correlation between $10D_q$ and $\alpha(F^k_{3d,3d})$ corresponding to spin-pairing energies for the d^7 system, illustrating that for mixed-spin complexes a multiple solution is possible. Furthermore, the results on the broadened data sets demonstrate that the adaptive grid algorithm was robust enough to find the solution in most cases, except in those cases for which the spectrum remains relatively unchanged with respect to small changes in the crystal field and electron−electron repulsion parameters. In such cases, the poor resolution seems to affect the outcome of the solutions or else the $L_{2,3}$-edge XAS is not sensitive enough to discard small variations in the crystal field.

In the analysis of the results of CaO and CaF_2 we tested three models, from which we recommend that whenever possible a different scaling factor for 2p−3d interactions should be used for direct Coulomb parameters $F^k_{2p,3d}$ and exchange interactions $G^k_{2p,3d}$. Then, for MnO, $LiMnO_2$, and Mn_2O_3 using simple crystal field models we were able to reproduce the experimental data remarkably well. Moreover, for $LiMnO_2$ we were able to obtain a very well defined ground state which resulted from a very large Jahn−Teller distortion, consistent with the observation of strain in batteries based on this material. Finally, in the case of Mn_2O_3 the simulations from two different types of Mn^{3+} was considered. The less abundant is a Mn^{3+} site in a nearly octahedral symmetry, while the most abundant type is a highly distorted Mn^{3+} site whose crystal field potential was modeled from the geometrical positions of the oxygen ligands. The results revealed that the distortion around the highly distorted site stabilizes a $^5T_2$, $(t_{2g})^2(e_g)^2$, state by maximizing the interaction of essentially the $3d_{xz}$ orbital with the most point charges. This state appeared to be practically pure and is not achievable in a nondistorted O_h site. Moreover, these results also showed that the ground state of the nondistorted site is a mixture of 84% ^5E and 16% $^3T_1$, in the fits more consistent with the actual composition of the material. The fitting of Mn_2O_3 using two simulations serves as an example that this methodology can be extended to the analysis of mixtures of doped materials or of naturally occurring materials with different metallic sites. However, like in the case of the analysis of the Co^{2+} data set, the methodology presented here is not capable of finding a unique solution for Mn_2O_3, finding instead a correlation for the $10D_q/\alpha(F^k_{3d,3d})$ ratio for the most viable fits, consistent with a mixture of spin states for the ground state of the O_h Mn^{3+} sites. This example also shows that the presented methodology has important limitations whenever the studied spectrum is relatively featureless and/or has a poor resolution. Finally, the case of Mn_2O_3 also illustrates how crystal-field potentials can be directly evaluated from geometrical models to study the electronic structure in highly distorted environments such as those appearing in many biological systems. This could shed light on differences in reactivity based on specific electronic structures optimized for a function that are a consequence of specific protein environments. In this case, we have optimized an effective nuclear charge, the ζ_{3d} radial hydrogen-like function given by eq 20, thus effectively using a single-ζ level of theory to be able to evaluate the radial part of the crystal-field potential, given by eq 38. This, however, can also be extended to calculate the crystal field parameters of eqs 17−19 and the values of Slater integrals of eqs 14−16, all from common radial 3d and/or common radial 2p functions using higher levels of theory (other than single-ζ). This is the subject of future contributions, for which other radial functions with different shapes (such as those used in density functional theory calculations) can be employed and their parameters optimized with respect to experimental data or, alternatively, use DFT models as a base for multiplet simulations.

The methodology presented here is currently being extended to streamline in a similar way the use of charge transfer multiplet simulations to analyze and interpret X-ray data from which covalency could also be obtained and from which radial functions can be further used to directly evaluate the value of hopping parameters. The work presented here explores cases for the first-row transition metals but could be easily extended to other transition metals, as the matrices for all operators are all the same and they only depend on the number of d electrons. What would be different are the values for the atomic parameters, which can be easily calculated by other codes.[26] The extension, however, to other spectroscopic techniques and to lanthanides is under current development.

One potential issue that we anticipate in the extension of this methodology to charge transfer multiplet simulations is the increase in the number of parameters, which will then increase the grid size and the overall computation time. However, it is evident that certain spectroscopies such as XPS and XES are very sensitive to covalency and to charge transfer and their inclusion is really important, especially for molecular systems with different types of bonding. Another issue is the possibility of overparameterization, but this is something that depends a great deal on the resolution of the data to analyze and the insensitivity of the spectroscopy for certain types of parameters, instead of the adaptive grid algorithm discussed here. In this regard, the inclusion of different types of available experimental spectra as well as the corresponding fit model, all at once, would increase the sensitivity for more types of parameters and would then reduce the chances of over-parameterization. In addition to this, the idea of calculating all radial parameters for all interactions involved in a particular system, using common radial functions, will redirect the problem of optimizing the parameters in the radial functions in a cohesive way, as opposed to the optimization of independent radial parameters. This redirection of the problem would produce more coherent solutions among all the different radial parameters. This type of strategy would be especially valuable if the number of radial parameters to fit is too large.

https://doi.org/10.1021/acs.inorgchem.2c02830
Inorg. Chem. 2023, 62, 3738−3760

Finally, in the application of the adaptive grid algorithm to charge transfer multiplet simulations, an important aspect to assess is the possibility of multiple solutions between, for example, charge transfer parameters and between crystal field parameters and charge transfer parameters and their importance and significance in terms of the electronic structure of the studied systems. This is also the subject of future studies in our group.

■ ASSOCIATED CONTENT

Supporting Information

The Supporting Information is available free of charge at https://pubs.acs.org/doi/10.1021/acs.inorgchem.2c02830.

Character table and a corresponding table for direct products for the O' double group discussed here, additional figures and tables to support the results of the fits discussed here, and a quick tutorial to implement and run optimizations of crystal-field multiplet simulations using BlueprintXAS (PDF)

■ AUTHOR INFORMATION

Corresponding Author

Mario U. Delgado-Jaime − *Department of Chemistry, University of Guadalajara, 44430 Guadalajara Jal., México;* orcid.org/0000-0003-4680-2001; Email: mario.delgado0665@academicos.udg.mx

Authors

María G. Herrera-Yáñez − *Department of Chemistry, University of Guadalajara, 44430 Guadalajara Jal., México*

J. Alberto Guerrero-Cruz − *Department of Chemistry, University of Guadalajara, 44430 Guadalajara Jal., México;* Present Address: Hylleraas Centre for Quantum Molecular Sciences, University of Oslo, Oslo 0315, NO, Norway

Mahnaz Ghiasi − *Inorganic Chemistry and Catalysis, Debye Institute for Nanomaterials Science, Utrecht University, 3584CG Utrecht, The Netherlands*

Hebatalla Elnaggar − *Inorganic Chemistry and Catalysis, Debye Institute for Nanomaterials Science, Utrecht University, 3584CG Utrecht, The Netherlands; Institut de Minéralogie, de Physique des Matériaux et de Cosmochimie (IMPMC), Sorbonne Université, UMR CNRS 7590, Université Pierre et Marie Curie, 75052 Paris Cedex 05, France;* orcid.org/0000-0002-4223-4054

Andrea de la Torre-Rangel − *Department of Chemistry, University of Guadalajara, 44430 Guadalajara Jal., México*

L. Alejandra Bernal-Guzmán − *Department of Chemistry, University of Guadalajara, 44430 Guadalajara Jal., México*

Roberto Flores-Moreno − *Department of Chemistry, University of Guadalajara, 44430 Guadalajara Jal., México;* orcid.org/0000-0001-5060-1363

Frank M. F. de Groot − *Inorganic Chemistry and Catalysis, Debye Institute for Nanomaterials Science, Utrecht University, 3584CG Utrecht, The Netherlands;* orcid.org/0000-0002-1340-2186

Complete contact information is available at: https://pubs.acs.org/10.1021/acs.inorgchem.2c02830

Notes

The authors declare no competing financial interest.

■ ACKNOWLEDGMENTS

M.G.H.-Y., J.A.G.-C., A.d.l.T.-R., L.A.B.-G., and M.U.D.-J. thank CONACyT for financial support under grant number A1-S-8384 and also thankfully acknowledge the computer resources, technical expertise, and support provided by the Laboratorio Nacional de Supercómputo del Sureste de México, CONACYT member of the network of national laboratories.

■ REFERENCES

(1) de Groot, F. M. F. Multiplet effects in X-ray spectroscopy. *Coord. Chem. Rev.* **2005**, *249*, 31−63.

(2) Glatzel, P.; Bergmann, U. High resolution 1s core hole X-ray spectroscopy in 3d transition metal complexes—electronic and structural information. *Coord. Chem. Rev.* **2005**, *249*, 65−95.

(3) Cowan, R. D. *The Theory of Atomic Structure and Spectra*; University of California Press: 1981.

(4) Butler, P. H. *Point Group Symmetry: Applications, Methods and Tables*; Plenum Press: 1981.

(5) Thole, B. T.; van der Laan, G. Branching ratio in x-ray absorption spectroscopy. *Phys. Rev. B* **1988**, *38*, 3158−3171.

(6) Thole, B. T.; van der Laan, G.; Butler, P. H. Spin-mixed ground state of Fe phthalocyanine and the temperature-dependent branching ratio in X-ray absorption spectroscopy. *Chem. Phys. Lett.* **1988**, *149*, 295−299.

(7) Haverkort, M. W. Quanty for core level spectroscopy - excitons, resonances and band excitations in time and frequency domain. *J. Phys.: Conf. Ser.* **2016**, *712*, 012001.

(8) Haverkort, M. W.; Zwierzycki, M.; Andersen, O. K. Multiplet ligand-field theory using Wannier orbitals. *Phys. Rev. B* **2012**, *85*, 165113.

(9) Delgado-Jaime, M. U.; Mewis, C. P.; Kennepohl, P. Blueprint XAS: a Matlab-based toolbox for the fitting and analysis of XAS spectra. *J. Synchrotron Radiation* **2010**, *17*, 132−137.

(10) Delgado-Jaime, M. U.; Kennepohl, P. Development and exploration of a new methodology for the fitting and analysis of XAS data. *J. Synchrotron Radiation* **2010**, *17*, 119−128.

(11) de Groot, F. M. F.; Kotani, A. *Core Level Spectroscopy of Solids*; CRC Press, :2008.

(12) van Vleck, J. The Jahn-Teller Effect and Crystalline Stark Splitting for Clusters of the Form XY_6. *J. Chem. Phys.* **1939**, *7*, 72−84.

(13) Gerloch, M.; Slade, R. *Ligand Field Parameters*; Cambridge University Press: 2009.

(14) Butler, P. H. *Point group symmetry applications: methods and tables*; Plenum Press: 1981.

(15) Thole, B. T.; Cowan, R. D.; Sawatzky, G. A.; Fink, J.; Fuggle, J. C. New probe for the ground-state electronic structure of narrow-band and impurity systems. *Phys. Rev. B* **1985**, *31*, 6856−6858.

(16) Wasinger, E.; de Groot, F.; Hedman, B.; Hodgson, K.; Solomon, E. L-edge X-ray Absorption Spectroscopy of Non-Heme Iron Sites: Experimental Determination of Differential Orbital Covalency. *J. Am. Chem. Soc.* **2003**, *125*, 12894−12906.

(17) Hocking, R. K.; Wasinger, E. C.; de Groot, F. M. F.; Hodgson, K. O.; Hedman, B.; Solomon, E. I. Fe L-edge XAS Studies of $K_4[Fe(CN)_6]$ and $K_3[Fe(CN)_6]$: A Direct Probe of Back-Bonding. *J. Am. Chem. Soc.* **2006**, *128*, 10442−10451.

(18) Hocking, R. K.; Wasinger, E. C.; Yan, Y.-L.; deGroot, F. M. F.; Walker, F. A.; Hodgson, K. O.; Hedman, B.; Solomon, E. I. Fe L-Edge X-ray Absorption Spectroscopy of Low-Spin Heme Relative to Non-heme Fe Complexes: Delocalization of Fe d-electrons into the Porphyrin Ligand. *J. Am. Chem. Soc.* **2007**, *129*, 113−125. PMID: 17199290

(19) Baker, M. L.; Mara, M. W.; Yan, J. J.; Hodgson, K. O.; Hedman, B.; Solomon, E. I. Solomon, E. I. K- and L-edge X-ray absorption spectroscopy (XAS) and resonant inelastic X-ray scattering (RIXS) determination of differential orbital covalency (DOC) of transition metal sites. *Coord. Chem. Rev.* **2017**, *345*, 182−208.

(20) Lundberg, M.; Kroll, T.; DeBeer, S.; Bergmann, U.; Wilson, S. A.; Glatzel, P.; Nordlund, D.; Hedman, B.; Hodgson, K. O.; Solomon,

E. I. Metal-Ligand Covalency of Iron Complexes from High-Resolution Resonant Inelastic X-Ray Scattering. *J. Am. Chem. Soc.* **2013**, *135*, 17121−17134.
(21) Kroll, T.; Hadt, R. G.; Wilson, S. A.; Lundberg, M.; Yan, J. J.; Weng, T.; Sokaras, D.; Alonso-Mori, R.; Casa, D.; Upton, M. H.; Hedman, B.; Hodgson, K. O.; Solomon, E. I. Resonant Inelastic X-ray Scattering on Ferrous and Ferric Bis-imidazole Porphyrin and Cytochrome c: Nature and Role of the Axial Metionine-Fe Bond. *J. Am. Chem. Soc.* **2014**, *136*, 18087−18099.
(22) Kroll, T.; Baker, M. L.; Wilson, S. A.; Lundberg, M.; Juhin, A.; Arrio, M.; Yan, J. J.; Bee, L. B.; Braun, A.; Weng, T.; Sokaras, D.; Hedman, B.; Hodgson, K. O.; Solomon, E. I. Effect of 3d/4p Mixing on 1s2p Resonant Inelastic X-ray Scattering: Electronic Structure of Oxo-Bridged Iron Dimers. *J. Am. Chem. Soc.* **2021**, *143*, 4569−4584.
(23) Zaanen, J.; Sawatzky, G.; Allen, J. W. Band gaps and electronic structure of transition-metal compounds. *Phys. Rev. B* **1985**, *55*, 418.
(24) Zaanen, J.; Westra, C.; Sawatzky, G. Determination of the electronic structure of transition-metal compounds: 2p x-ray photo-emission spectroscopy of the nickel dihalides. *Phys. Rev. B* **1986**, *33*, 8060.
(25) van der Laan, G.; Westra, C.; Haas, C.; Sawatzky, G. A. Satellite structure in photoelectron and Auger spectra of copper dihalides. *Phys. Rev. B* **1981**, *23*, 4369−4380.
(26) Cowan, R. D. *The Theory of Atomic Structure and Spectra*; University of California Press: 1981.
(27) Haverkort, M. W. Quanty for core level spectroscopy - excitons, resonances and band excitations in time and frequency domain. *J. Phys.: Conf. Ser.* **2016**, *712*, 012001.
(28) Tanaka, A.; Jo, T. Resonant 3d, 3p and 3s Photoemission in Transition Metal Oxides Predicted at 2p Threshold. *J. Phys. Soc. Jpn.* **1994**, *63*, 2788−2807.
(29) Fernández-Rodríguez, J.; Toby, B.; van Veenendaal, M. Xclaim: A graphical interface for the calculation of core-hole spectroscopies. *J. Electron Spectrosc. Relat. Phenom.* **2015**, *202*, 81−88.
(30) Stepanow, S.; Lodi Rizzini, A.; Krull, C.; Kavich, J.; Cezar, J. C.; Yakhou-Harris, F.; Sheverdyaeva, P. M.; Moras, P.; Carbone, C.; Ceballos, G.; Mugarza, A.; Gambardella, P. Spin Tuning of Electron-Doped Metal−Phthalocyanine Layers. *J. Am. Chem. Soc.* **2014**, *136*, 5451−5459.
(31) Vorwerk, C.; Cocchi, C.; Draxl, C. Addressing electron-hole correlation in core excitations of solids: An all-electron many-body approach from first principles. *Phys. Rev. B* **2017**, *95*, 155121.
(32) Ramanantoanina, H.; Daul, C. A non-empirical calculation of 2p core-electron excitation in compounds with 3d transition metal ions using ligand-field and density functional theory (LFDFT). *Phys. Chem. Chem. Phys.* **2017**, *19*, 20919−20929.
(33) Pinjari, R. V.; Delcey, M. G.; Guo, M.; Odelius, M.; Lundberg, M. Restricted active space calculations of L-edge X-ray absorption spectra: From molecular orbitals to multiplet states. *The Journal of Chemical Physics* **2014**, *141*, 124116.
(34) Guo, M.; Källman, E.; Pinjari, R. V.; Couto, R. C.; Kragh Sørensen, L.; Lindh, R.; Pierloot, K.; Lundberg, M. Fingerprinting Electronic Structure of Heme Iron by ab initio Modeling of Metal L-edge X-ray Absorption Spectra. *Journal of Chemical Theory and Computation* **2019**, *15*, 477−489.
(35) Roemelt, M.; Maganas, D.; DeBeer, S.; Neese, F. A combined DFT and restricted open-shell configuration interaction method including spin-orbit coupling: Application to transition metal L-edge X-ray absorption spectroscopy. *The Journal of Chemical Physics* **2013**, *138*, 204101.
(36) Maganas, D.; DeBeer, S.; Neese, F. Restricted Open-Shell Configuration Interaction Cluster Calculations of the L-edge X-ray Absorption Study of TiO_2 and CaF_2 Solids. *Inorganic Chemistry* **2014**, *53*, 6374−6385. PMID: 24871209
(37) Maganas, D.; DeBeer, S.; Neese, F. Pair Natural Orbital Restricted Open-Shell Configuration Interaction (PNO-ROCIS) Approach for Calculating X-ray Absorption Spectra of Large Chemical Systems. *The Journal of Physical Chemistry A* **2018**, *122*, 1215−1227.
(38) Ceder, G.; der Ven, A. V.; Marianetti, C.; Morgan, D. First-principles alloy theory in oxides. *Modelling and Simulation in Materials Science and Engineering* **2000**, *8*, 311−321.
(39) Zhu, X.; Meng, F.; Zhang, Q.; Xue, L.; Zhu, H.; Lan, S.; Liu, Q.; Zhao, J.; Zhuang, Y.; Guo, Q.; Liu, B.; Gu, L.; Lu, X.; Ren, Y.; Xia, H. $LiMnO_2$ cathode stabilized by interfacial orbital ordering for sustainable lithium-ion batteries. *Nature Sustainability* **2021**, *4*, 392−401.
(40) Yaghoobnejad Asl, H.; Manthiram, A. Toward sustainable batteries. *Nature Sustainability* **2021**, *4*, 379−380.
(41) Ballhausen, C. *Introduction to Ligand Field Theory*; McGraw Hill: 1962.
(42) Coster, D.; L. Kronig, R. D. New type of auger effect and its influence on the x-ray spectrum. *Physica* **1935**, *2*, 13−24.
(43) de Groot, F. *X-ray Absorption of Transition Metal Oxides*; Radboud University Nijmegen: 1991.
(44) Delgado-Jaime, M. U.; Zhang, K.; Vura-Weis, J.; de Groot, F. M. F. CTM4DOC: electronic structure analysis from X-ray spectroscopy. *J. Synchrotron Radiation* **2016**, *23*, 1264−1271.
(45) Miedema, P.; Ikeno, H.; de Groot, F. M. F. First principles multiplet calculations of the calcium $L_{2,3}$ x-ray absorption spectra of CaO and CaF_2. *J. Phys.: Condens. Matter* **2011**, *23*, 145501−145507.
(46) Qiao, R.; Chin, T.; Harris, S. J.; Yan, S.; Yang, W. Spectroscopic fingerprints of valence and spin states in manganese oxides and fluorides. *Current Applied Physics* **2013**, *13*, 544−548.
(47) Griffith, J. On the stabilities of transition metal complexes—I Theory of the energies. *Journal of Inorganic and Nuclear Chemistry* **1956**, *2*, 1−10.
(48) Griffith, J. On the stabilities of transition metal complexes—II Magnetic and thermodynamic properties. *Journal of Inorganic and Nuclear Chemistry* **1956**, *2*, 229−236.
(49) Orgel, L. E. Electronic Structures of Transition-Metal Complexes. *The Journal of Chemical Physics* **1955**, *23*, 1819−1823.
(50) König, E.; Kremer, S. Exact Spin-Pairing Energies at the Crossovers in Octahedral d^4, d^5, d^6, and d^7 Transition Metal Complexes. *Theoret. Chim. Acta (Berl.)* **1971**, *23*, 12−20.
(51) van Schooneveld, M. M.; Kurian, R.; Juhin, A.; Zhou, K.; Schlappa, J.; Strocov, V. N.; Schmitt, T.; de Groot, F. M. F. Electronic Structure of CoO Nanocrystals and a Single Crystal Probed by Resonant X-ray Emission Spectroscopy. *The Journal of Physical Chemistry C* **2012**, *116*, 15218−15230.
(52) van der Laan, G.; Zaanen, J.; Sawatzky, G. A.; Karnatak, R.; Esteva, J.-M. Comparison of x-ray absorption with x-ray photo-emission of nickel dihalides and NiO. *Phys. Rev. B* **1986**, *33*, 4253−4263.
(53) Bagtache, R.; Brahimi, R.; Abdmeziem, K.; Trri, M. Physical properties of o-$LiMnO_2$. *Appl. Phys. A: Mater. Sci. Process.* **2019**, *125*, 606.
(54) Pauling, L.; Shappell, M. D. The Crystal Structure of Bixbyite and the C-Modification of the Sesquioxides. *Zeitschrift für Kristallographie - Crystalline Materials* **1930**, *75*, 128−142.
(55) Roth, N.; Ye, F.; May, A. F.; Chakoumakos, B. C.; Iversen, B. B. Magnetic correlations and structure in bixbyite across the spin-glass transition. *Phys. Rev. B* **2019**, *100*, 144404.
(56) Mathew, K.; Zheng, C.; Winston, D.; Chen, C.; Dozier, A.; Rehr, J. J.; Ong, S. P.; Persson, K. A. High-throughput computational X-ray absorption spectroscopy. *Scientific Data* **2018**, *5*, 180151.
(57) Regulski, M.; Przenioslo, R.; Sosnowska, I.; Hohlwein, D.; Schneider, R. Neutron diffraction study of the magnetic structure of $\alpha - Mn_2O_3$. *J. Alloys Compd.* **2004**, *362*, 236−240.

https://doi.org/10.1021/acs.inorgchem.2c02830
Inorg. Chem. 2023, 62, 3738−3760